A Novel Population of Slow Magnetosonic Waves and a Method for the Observation of the Roots of Plasma Bubbles in the Lower Ionosphere

Charles Lougheed Bennett[1,1]

[1]Lawrence Livermore National Laboratory

April 4, 2023

Abstract

Using data from the Van Allen Probe and Swarm-Bravo satellites, evidence for a persistent population of slow magnetosonic waves in the ionosphere is presented. Dispersion relations from two-fluid analyses of waves in warm plasma are used to interpret and explicate these observations. These waves appear to be continuously present and globally distributed. Their amplitudes systematically decrease with increasing altitude. The amplitudes are also correlated with longitude in a manner consistent with the global distribution of lightning strikes. Evidence for narrow resonances in the Swarm data consistent with doppler shifted Schumann resonance frequencies is presented. In addition, nearly dispersionless fast magnetosonic waves are sometimes also seen. A new method for the analysis of these waves suggests they show the existence of "foamy" plasma bubble "roots" at the base of the ionosphere.

A Novel Population of Slow Magnetosonic Waves and a Method for the Observation of the Roots of Plasma Bubbles in the Lower Ionosphere

Charles L. Bennett[1]

[1]Retired from Lawrence Livermore National Laboratory.

Corresponding author: Charles L. Bennett (Charlie_Bennett@comcast.net)

Key Points:

- Globally distributed slow magnetosonic waves in the ionosphere have been found with amplitudes decreasing vs altitude
- It is suggested that these are produced by lightning generated waves impacting the Earth Ionosphere waveguide upper boundary
- Unusual low dispersion whistlers suggest the existence of plasma depletion "roots" extending to the base of the ionosphere

Abstract

Using data from the Van Allen Probe and Swarm-Bravo satellites, evidence for a persistent population of slow magnetosonic waves in the ionosphere is presented. Dispersion relations from two-fluid analyses of waves in warm plasma are used to interpret and explicate these observations. These waves appear to be continuously present and globally distributed. Their amplitudes systematically decrease with increasing altitude. The amplitudes are also correlated with longitude in a manner consistent with the global distribution of lightning strikes. Evidence for narrow resonances in the Swarm data consistent with doppler shifted Schumann resonance frequencies is presented. In addition, nearly dispersionless fast magnetosonic waves are sometimes also seen. A new method for the analysis of these waves suggests they show the existence of “foamy” plasma bubble “roots” at the base of the ionosphere.

Plain Language Summary

Using satellite data, just as the acoustic noise from distant lightning is heard to rumble, sometimes a considerable time later, for a much longer duration than the visible flashes, an even more greatly delayed and spread-out series of plasma-sound waves are found in the earth’s ionosphere after every lightning bolt. The noise of these plasma-sound waves comes in two forms. One set of plasma-sound waves is slow and is found to be always present over the entire globe. Properly accounting for this noise in satellite electromagnetic field measurements could improve the quality of measurements of the earth’s magnetic field from space, and lead to a better understanding of our earth’s magnetic field and its ionosphere. A second set of plasma-sound waves is fast, and more sporadic in appearance. These fast plasma-sound waves are associated with plasma bubbles that can interfere with radio wave communications around the globe. Better understanding these fast waves and bubbles could possibly allow for better radio communication processes.

1 Introduction

The mean global rate of lightning is 60 flashes/s (Burgesser, 2017) and is concentrated most strongly in the mid-latitude continental regions. The high global rate of lightning strokes, together with the low attenuation at low frequencies leads to the establishment of standing wave resonances within the Earth Ionospheric Waveguide (EIWG). Within the EIWG, the wave attenuation in the frequency range below 100 Hz is roughly 0.5 dB/Mm according to (Chapman et al.,1966), so that such low frequency waves may travel several times around the globe before losing most of their energy. The propagation of electromagnetic waves in the EIWG is discussed most extensively by Nickolaenko and Hayakawa (2002), see also (Budden, 1957; Jackson, 1975; Schumann, 1952). The resonances of the EIWG are known as the Schumann resonances (SRs). The transient vertical electric and horizontal magnetic fields at great distances from an individual strong lightning stroke, designated Q-bursts by (Ogawa et al., 1967), appear as bipolar pulses in the time domain according to Nickolaenko et al. (2004), comprising a series of diminishing intensity delayed pulses corresponding to multiple Earth circuits.

If the EIWG was a lossless, perfectly spherical cavity, the SR eigenfrequencies would be

$$f_n = \frac{c}{2\pi R_e}\sqrt{n(n+1)}\,, \tag{1}$$

where R_e is the Earth’s radius, c is the speed of light and n is the number of the eigenmode. In the actual EIWG, the frequencies of the lowest eigenmodes are only slightly lower than the values given by equation 1, with observed values for the five lowest eigenmodes of 7.8, 14.1, 20.3, 26.3 and 32.5 Hz as listed in table 1 of (Chapman et al., 1966). The corresponding quality factor Q values are 4, 4.5, 5, 5.5 and 6 for these resonances. Q values for a resonance at a given frequency are commonly defined as the ratio of the resonance frequency to the width of the resonance. The SR intensities observed at a fixed location have significant diurnal and seasonal variations in amplitude, sometimes over a factor of two (Fullekrug M. , 1995) as the global rate of lightning varies as the subsolar point crosses the three main continental regions (Rodriguez-Camacho et al., 2021; Satori, 1996). From the quality of the correlation between the observed intensity of the SRs and the instantaneous lightning rate (Boldi et al., 2017) no evidence is found for contributions other than lightning to the intensity of the SRs in the EIWG. Measurements of the magnetic field intensity of the lowest SR at ground level are typically less than 1 $pT/Hz^{1/2}$, e.g. (Boldi et al., 2017; Fullekrug, 1995; Fullekrug & Fraser-Smith, 1996; Price, 2016; Rodriguez-Camacho et al., 2021; Salinas et al., 2016; Sentman, 1987).

Some portion of the low frequency electromagnetic energy of the SRs may penetrate through the EIWG upper boundary (EIWGUB) in the form of plasma waves. Evidence for this was sought and first claimed by (Ni & Zhao, 2005) based on measurements of electric and magnetic field data from the Aureol-3 satellite. The Aureol-3 satellite polar orbit covered an altitude range from 400 km to 2,000 km with an inclination of 82.5°. The claims of Ni and Zhao were not believed by (Surkov et al., 2013) for a couple of reasons. First, the Ni and Zhao spectral amplitudes at 8 Hz were *thought* to be too high: B ~ 45 $pT/Hz^{1/2}$ and E ~ 20 $\mu V/m/Hz^{1/2}$. Second, the peak frequencies seen in the magnetic fields did not match SR frequencies measured at ground level. However, Surkov et al., (2013) did not consider either the profound impact of doppler shifts on the SR frequencies or the possibility of passage through plasma bubbles. It will be shown below that these factors could possibly have played a role in the Ni and Zhao observations.

Later analysis by (Simoes et al., 2011) of electric field data from the C/NOFS satellite provided a more compelling case for the presence of SR electric field signatures in the ionosphere. The C/NOFS satellite had a 401 km perigee, 852 km apogee and 13° inclination. These signatures were observed throughout the ~3-year lifetime of the C/NOFS satellite with a typical electric field spectral density of 0.3 $(\mu V/m)/Hz^{1/2}$, which is nearly three orders of magnitude weaker than the observations near the earth's surface of the SR standing wave amplitudes. The great weakness of the ionospheric electric field SRs observed by (Simoes et al., 2011) is consistent with the (Surkov et al., 2013) calculation.

The three Swarm satellites, *Alpha*, *Bravo* and *Charlie*, (SwA, SwB and SwC) launched in November 2013 by the European Space Agency had the mission objective to provide the best ever survey of the geomagnetic field and its temporal evolution, (Friss-Christensen et al., 2006). In a comparison (Finlay et al., 2020) of the quality of the agreement between a sophisticated model of the time-dependent near-earth geomagnetic field and the Swarm, CryoSat-2, CHAMP, SAC-C and Oersted satellites, the Swarm data indeed had the smallest rms differences between model and observations. The mean Swarm rms value for along-track field differences over all three satellites and all three field components was only 0.26 nT, while CHAMP's mean was 0.39 nT. The high quality of the Swarm magnetic field measurements was achieved despite early challenges with unexpected Sun-driven disturbances (Toffner-Clausen et al., 2016).

At 21:01:30 on 14 March 2014 two days after SwB was raised to its operational altitude of 525 km, a mysterious chirping in the high rate SwB VFM-y channel data suddenly appeared.

Exactly at the time that this chirping appeared, the overall noise level also suddenly increased slightly. This and every other time in this article not explicitly labeled as Local Solar Time (LST) is given as Universal Time (UT). This overall noise level was not significantly different between the dayside and nightside of the orbits and did not depend on longitude. The mysterious chirping just as suddenly ceased at 11:17:53 on 25 June 2014. The cessation of chirping coincided with a manual power cycling of the VFM instrument on SwB. According to (European Space Research and Technology Centre, 2018), at the time that the chirping disappeared from the data, it is stated "70pT noise in y-measurement since [14 March 2014]". After this power cycling, the overall background noise level in the y channel returned to that seen before the onset of chirping. The overall background noise levels in the x and z channels did not significantly change after the power cycle. It will be suggested below that this mysterious chirping might be associated with SRs.

Throughout the CHAMP satellite mission, a mysterious chirping noise feature was found (Yin et al., 2015), having so called "W" and "V" shaped variations in spectrograms like those seen in the SwB data described in the previous paragraph with a similar amplitude. This chirping was found to be correlated with regions of small magnetic declination, but it was stated "This good correlation between the two very different quantities suggest that the V- and W-shaped signals in the By component are artificial". Yin et al. (2015) state: "we strongly suggest that it [the mysterious chirping] reflects an oscillation of the y-component ADC at the crossover from negative to positive readings." Beyond this explanation for the correlation between W- and V-shaped events and small magnetic declination, there is no detailed explanation for the shape of these features. In the present paper, the same model that describes the SwB chirping also quantitatively reproduces the shape of both the V- and W-shaped events in the CHAMP data.

Although primarily designed to study the magnetosphere (Mauk et al., 2013) rather than the ionosphere, the perigee of the Van Allen Probes A and B (VAP-A and VAP-B) of approximately 575 km is close to the SwB altitude. In the last months of the VAP mission in 2019, the perigees of VAP-A and VAP-B were lowered to approximately 275 km and lower ionospheric data were acquired. Because of the higher sensitivity and higher sampling rate of the VAP-A & B Electric and Magnetic Field Instrument Suite (EMFISIS) (Kletzing et al., 2013) detectors, near perigee these data can be used to investigate and corroborate the nature of the mysterious SwB chirping and to detect plasma depletion regions (PDRs) or plasma bubbles. The "roots" of PDRs are defined as depletion regions that extend all the way to the bottom of the ionosphere.

Plasma bubbles were originally suggested by Woodman and Hoz (1976) to explain plumelike features in ionospheric irregularities responsible for the Spread-F phenomenon in the F-layer of the ionosphere (Woodman, 2009) and may be observed by various techniques. Radar observations of plasma bubbles (e.g. Abdu et al., 2012; Hysell et al., 2005; Kudeki & Bhttacharyya, 1999; Narayanan et al., 2014; Patra et al., 2005; Tsunoda, 1983; Yokoyama et al., 2011) require the presence of ionospheric irregularities having sizes comparable to the radar wavelength. Without the conversion of large-scale density variations to small-scale irregularities such as can be produced by turbulent activity, the presence of possible non-turbulent PDR roots at the bottom of the ionosphere prior to the process of buoyant rising in the form of bubbles through the E- and F-layers of the ionosphere is unlikely to be detected by radar. Plasma bubbles may alternatively be detected as emission depletion bands in optical observations, (e.g., Immel et al., 2003; Kil et al., 2004; Makela & Kelley, 2003; Martinis et al., 2003; Mendillo &

Baumgardner, 1982; Pimenta et al., 2003; Shiokawa et al., 2004). Recent observations (Adkins & England, 2022; Karan et al., 2020) of plasma bubbles as seen in the far-ultraviolet under the Global-scale Observations of the Limb and Disk (GOLD) satellite enable detailed occurrence rate, drift rate and separation measurements. The conjunction of in-situ SWARM measurements with GOLD observations of plasma depletions (Rodriguez-Zuluaga et al., 2020) demonstrates the validity of the GOLD detections of plasma bubbles. However, none of these methods: radar, optical or in-situ satellite measurements (necessarily restricted to sustainable orbits) are sensitive to *non-turbulent* depletions in the plasma density at the interface between the neutral atmosphere and the bottom of the ionosphere. In discussing the benefits of very low earth orbit (Crisp et al. 2020) show in their Figure 4 that at altitudes below 200 km, orbital lifetimes drop to mere days at best.

Rocket experiments (Abdu et al., 1991; Hysell et al., 2005) are capable of in situ probing in this region, but they obviously have extremely limited spatial and temporal coverage. In one typical case of a rocket flight coincident with developing spread F radar observations (Hysell et al., 2005) observe strong electron density variations at an altitude of about 100 km, c.f. their Figure 2, while at the same time substantial coherent scatter from irregularities is seen near 100 km, c.f. their Figure 1, but the rocket and radar observations are not at the same location. In the present work, a novel method is presented for the detection and analysis of non-turbulent PDR roots undetectable by any other observational method known to this author.

In this article, evidence is presented that the mysterious SwB chirping as well as the CHAMP chirping could be associated with a globally distributed population of slow magnetosonic waves present throughout the ionosphere that is also seen in VAP data. To this author's knowledge, this population has not been previously recognized in the literature. It is suggested that these are lightning generated waves that have been partially converted to slow magnetosonic waves upon passage into the ionosphere. In **section 2** of the present work, a discussion of various theoretical models is given to better understand and interpret the satellite observations. First, the two-fluid model of De Jonghe & Keppens (2020a) is reviewed as it provides an illuminating picture of the nature of the plasma waves that may propagate in the ionosphere. Then the importance of doppler shift effects for plasma waves having speeds comparable to or much less than satellite speeds is discussed. Concluding the theoretical section, an overview of the propagation of Lightning Generated (LG) waves from strike to satellite is presented. In **section 3** analysis of data from the VAP satellite mission leads to the conclusion that slow magnetosonic noise is present in the ionosphere throughout the seven-year lifetime of the VAP mission. In **section 4** analysis of the Swarm data is provided. It is suggested that the mysterious chirping is consistent in frequency with Schumann resonances that have been doppler shifted by the relative velocity between satellite and waves.

2 Theoretical Analysis

2.1 Two Fluid Plasma Model

In De Jonghe and Keppens (2020a), using a fully relativistic treatment for a two-fluid warm ion-electron plasma, a polynomial dispersion relation of sixth degree in the squared frequency ω^2 and fourth degree in squared wavenumber k^2 results. This dispersion relation is a function of five parameters: the electron and ion cyclotron frequencies, the electron and ion sound speeds and the propagation angle between the wavevector **k** and the ambient magnetic field $\mathbf{B_0}$ vector. These authors provide comprehensive expressions for the polynomial coefficients in terms of these five parameters, so that explicit solutions to the dispersion relation are found for a given wavenumber as roots of the sixth order polynomial in ω^2. It is shown in De Jonghe & Keppens (2020a) that for oblique propagation angles, the frequency ordering of the six modes corresponding to the six roots of the sixth order polynomial are fixed in the order

$$\omega_S \leq \omega_A \leq \omega_F \leq \omega_M \leq \omega_O \leq \omega_X. \quad (2)$$

The S, F and A labels refer to the Magnetohydrodynamic (MHD) slow magnetosonic (MS), fast MS and Alfven waves, while M stands for the modified electrostatic waves, O represents "ordinary" and X represents "extraordinary" electromagnetic modes. In the following discussion of the lower frequency waves propagating in the earth's ionosphere, only the MHD wave types are of present interest. In the figures and text these three MHD wave modes are green for ***S*** slow MS, red for ***A*** Alfven and blue for ***F*** fast MS waves. Representative dispersion relations using De Jonghe and Keppens (2020a) model for a typical ionospheric composition are shown in Figure **1**. The specific values shown were computed using the International Reference Ionosphere (IRI) model-2016 (Blilitza et al., 2016) estimates for the case of the data acquisition shown in Figure **5** below. For these conditions, the wave normal surfaces are shown in Figure **2** for frequencies below, near and above the transition between the short and long wavelength limits.

In Figure **1** four regions of dispersionless behavior are seen in **1c**, **1f** and **1i**: for a limited range of frequencies above Ω_x ***A*** waves are nearly dispersionless, and below Ω_x all three modes ***F***, ***A*** and ***S*** become dispersionless in the long wavelength limit. Five regions of dispersive or "whistling" behavior are seen: descending frequency ***F*** whistling above Ω_x, ascending frequency ***A*** whistling below and asymptotic to Ω_x from below, ascending frequency ***A*** whistling starting a few orders of magnitude above Ω_x, descending frequency ***A*** whistling above and asymptotic to Ω_x from above, and finally ascending frequency ***S*** whistling below and asymptotic to $\Omega_x\cos(\theta)$ from below. For typical ionospheric conditions, although the ***F*** wave dispersion constant depends on plasma density and magnetic field strength, it is relatively insensitive to ion species or temperature.

The specific angle choice in Figure **1** and the specific wavenumber choices in Figure **2** are chosen to illustrate the transitions in the nature of the wave propagation from long wavelength to short wavelength behavior for each of the wave types. It can be seen from **2a**, **2d** and **2g** for ***F*** waves that they undergo a transition from isotropic to anisotropic behavior as the wavenumber crosses the ion cyclotron resonance. In contrast, for both ***A*** and ***S*** waves in the low wavelength limit, c.f. (Goedbloed et al., 2019) Figure 5.3, energy only flows directly along magnetic field lines as the relation

$$V_p = V_g \cdot \cos(\theta) \quad (3)$$

between phase and group velocity holds. For ***A*** waves this relation is independent of temperature, while for ***S*** waves, this relation holds for ion thermal speeds much less than the speed of light.

2.2 Doppler Shifts

In general, the observed frequency of a plasma wave seen by an observer moving at velocity V_o ***relative to the plasma*** is

$$\omega_o = \omega - \boldsymbol{k} \cdot \boldsymbol{V}_o = \omega - k\, V_o\, \hat{\boldsymbol{k}} \cdot \hat{\boldsymbol{V}}_o \ . \tag{4}$$

The observed frequency relative to the emitted frequency can be written in terms of the magnitude of the phase velocity $V_p = \omega/k$ as

$$\frac{\omega_o}{\omega} = 1 - \frac{V_o\ \hat{\boldsymbol{k}} \cdot \hat{\boldsymbol{V}}_o}{V_p} . \tag{5}$$

For ***A*** and ***S*** wave types following equation 3, the observed to emitted doppler frequency ratio *DFR* is

$$DFR = \frac{\omega_o}{\omega} = 1 - \frac{V_o\ \hat{\boldsymbol{k}} \cdot \hat{\boldsymbol{V}}_o}{V_g\ \hat{\boldsymbol{k}} \cdot \hat{\boldsymbol{B}}_0} . \tag{6}$$

For $\hat{\boldsymbol{k}}$ uniformly but randomly distributed over all directions, and for an angle γ between $\hat{\boldsymbol{V}}_o$ and $\hat{\boldsymbol{B}}_0$, the probability distribution function pdf of *DFR* derived from expression 6 (details of this derivation are in the supporting information) is a Lorentzian function

$$pdf \propto \frac{1}{\left(DFR - 1 + \frac{V_o}{V_g}\cos(\gamma)\right)^2 + \left(\frac{V_o}{V_g}\sin(\gamma)\right)^2} . \tag{7}$$

Satellite speeds and possible plasma drift speeds in the ionosphere are so much less than *fast* plasma waves that their *DFR* values are only narrowly distributed about unity. In stark contrast, *slow* ionospheric plasma wave speeds may be comparable to (for H^+ plasmas) or substantially less than (for O^+ or NO^+ plasmas) ionospheric satellite speeds. For slow waves the distribution of *DFR* values is thus strongly dependent on the orbital inclination angle. For satellites in low inclination orbits, such as the Van Allen Probes, γ is nearly ±90°, so that *DFR* values are peaked near unity, but have distribution HWHM (half width at half max) = V_o/V_g values that may become very broad, such as for waves in a predominantly O^+ plasma. For satellites in nearly polar orbits, such as the Swarm satellites, γ is near 0° at the ascending node and near 180° at the descending node. In either case the widths, being proportional to sin(γ), are much narrower. As a result, for the Swarm satellites, near the ascending nodes, for slow H^+ plasma waves for which V_o/V_g is near unity, *DFR* values near 0 dominate, while near the descending nodes, *DFR* values near 2 are dominant. This rather surprising difference between ascending and descending nodes seems to appear in some Swarm satellite data, as discussed in **section 4**.

Finally, at the magnetic poles, occasionally crossed by satellites having high inclination orbits, the satellite velocity becomes perpendicular to the magnetic field direction, so that the mean *DFR* value become unity and the underlying frequencies of possible resonance may be seen, albeit with increased widths. The derivation of the Lorentzian distribution, based on the assumption of wavevectors uniformly distributed over all directions may no longer be valid in the polar region however, since lighting strikes are primarily concentrated in a band some tens of degrees wide about the equator. Thus, most lightning generated waves reaching the polar regions would have meridionally aligned wavevectors.

2.3 Random Phase Approximation for Phase Velocity

For the analysis of superpositions of large numbers of waves having uncorrelated phases the random phase approximation (RPA) has been found (Shapiro & Campillo, 2004) particularly useful. In RPA, off diagonal elements of spectral correlations are neglected. For the electric and magnetic components having frequency f, angular frequency $\omega = 2\pi f$, Faraday's law leads to

$$\boldsymbol{k} \times \boldsymbol{E}(\mathrm{f}) = \omega \boldsymbol{B}(\mathrm{f}). \tag{8}$$

Thus, the dot product of equation (8) with the conjugate magnetic field amplitude divided by the magnitude *k* of the wave vector in RPA leads to the expression

$$V_p = \omega/k = \widehat{\boldsymbol{k}} \times \boldsymbol{E}(\mathrm{f}) \cdot \boldsymbol{B}^*(\mathrm{f})/[\boldsymbol{B}(\mathrm{f}) \cdot \boldsymbol{B}^*(\mathrm{f})], \tag{9}$$

which can be written in terms of the angles α between $\widehat{\boldsymbol{k}}$ and $\widehat{\boldsymbol{E}}$ and β between $\widehat{\boldsymbol{k}} \times \widehat{\boldsymbol{E}}$ and $\widehat{\boldsymbol{B}}$ as

$$V_p = \sin(\alpha)\cos(\beta)\, |\boldsymbol{E}(\mathrm{f})|/|\boldsymbol{B}(\mathrm{f})| \leq |\boldsymbol{E}(\mathrm{f})|/|\boldsymbol{B}(\mathrm{f})| \ , \tag{10}$$

for the magnitude of the phase velocity. The ratio of electric to magnetic magnitudes thus provides an upper limit to V_p. From this expression, together with the observation that slow plasma wave speeds V_s are typically orders of magnitude less than fast plasma wave speeds V_f in the ionosphere, slow waves are more readily detected in the magnetic field amplitudes than in the electric field amplitudes and vice versa for fast waves.

2.4 Lightning Generated (LG) Energy Propagation into the Ionosphere

The energy produced by a lightning stroke passes through a wide variety of conditions as it propagates away from the source region and enters the ionosphere as illustrated in Figure **3**. Energy radiates away from the source in a complex pattern. Electromagnetic Pulses (EMPs) from a single lightning stroke in the near field region propagate approximately isotropically (above the earth's surface) at the speed of light for distances less than the height of the ionosphere. At distances up to a few 100 km, a complex superposition of direct and multipath waves is found with a great variety of waveforms (Wang et al. 2020). At greater distances, the Earth Ionosphere waveguide (EIWG) bounded by solid earth below and the EIWG upper boundary (EIWGUB) above, substantially affects EMP propagation, lowering its speed and acting as a low pass filter. According to (Nickolaenko et al., 2008), the expanding circular wavefront within the EIWG starts to converge after passing the "equatorial arc distance" of 10 Mm, reaches a local minimum amplitude at 15.5 Mm, then subsequently increases in amplitude from geometrical focusing, finally reaching a local maximum in intensity at the 20 Mm antipodal location. After passing the antipodal location, the circular wavefront again expands, passes the second equatorial distance, and again converges to return to the point of origin and repeat the cycle. Such "Q-burst" wave propagation following Nickolaenko et al. (2004) is illustrated in supplemental Figure **S1**. EMP propagation through the EIWG is well approximated by a speed of 245 Mm/s, as shown in Figure **S1**, along the arc distance through the EIWG.

Where conditions are conducive to penetration through the EIWGUB and continuation to an ionospheric detector, EMPs in the EIWG may convert to ***F*** mode plasma waves at the EIWGUB and travel along nearly vertical paths (Jacobson et al., 2011; Santolik et al., 2009) as indicated by the three upward directed blue arrows extending from the EIWGUB to the Van Allen probe altitude at three locations along its orbit in Figure **3**. Because conditions are not always conducive, not every EMP produces ***F*** waves observable by satellites in the ionosphere. The total propagation time ΔT from source to satellite detector may be written as the sum of the propagation time through the EIWG, ΔT_0 , and the remaining propagation time from the bottom of the ionosphere up to the satellite. As seen in Figures **1c**, **1f** and **1i**, the group velocity V_g in the ionosphere for frequencies above the relevant ion cyclotron frequency is proportional to the inverse square root of frequency. The group velocity is also proportional to $\sqrt{B/n_e}$ with electron density n_e and magnetic field strength B a function of distance along the traversed path. As a result ΔT may be written in terms of an overall dispersion constant DC as

$$\Delta T = \int \frac{ds}{V_g(s)} = \Delta T_0 + DC/\sqrt{f} \,, \tag{11}$$

where DC is proportional to the integral:

$$DC \propto \int \sqrt{n_e/B} \; ds \,. \tag{12}$$

The IRI values of n_e and B shown in Figure **4** may be used to compute DC values for vertically propagating ***F*** waves as a function of altitude. These IRI model estimates are compared with the dispersion constants determined from observed whistlers in the VAP data (as described below) for a representative perigee crossing in Figure **6g**. Most of the VAP observed *DC* values are found to be proportional to the IRI estimate, however, in certain cases unusually low values of dispersion are found.

The lower ionosphere is a highly complex region that sporadically exhibits plasma density fluctuations, such as plasma bubbles (PB) as described by (Woodman, 2009). PBs are extended regions of low-density plasma that tend to extend along magnetic field lines

(Rodriguez-Zuluaga et al., 2022). It is suggested here that the unusually low dispersion events in the scalogram data are observed when the VAP happens to be in a plasma bubble**.** Evidence that PBs may sometimes extend to the base of the ionosphere, as illustrated in Figure **3** is shown by the observation of Q-burst waveforms that have suffered no discernible extra dispersion beyond that already accounted for in the Q-burst waveform.

In Figure **4**, the plasma conditions computed using the IRI model (Bilitza et al., 2016) are shown as a function of altitude for a representative time and location corresponding to the data shown in Figures **5**, **6** and **7** at the altitude highlighted with asterisks in Figure **4**. The magnetic field in this IRI model is given by IGRF-13 coefficients (Alken et al., 2021). Also shown in this figure are the two-fluid estimates for the fast and slow MS speeds V_f and V_s as a function of ion species. Because there are generally one or more local minima in V_f as a function of altitude, "trapping regions" (Chen & Thorne, 2012) such as indicated by the horizontal dashed line in **4d**, may form, within which plasma waves may reflect one or more times between upper and lower altitude limits. Such reflections can produce "echoes" (Chum et al., 2009) such as those appearing in Figure **5**.

In contrast to ***F*** waves, low frequency ***S*** and ***A*** waves travel paths constrained to follow magnetic field lines. One such representative field line is indicated in Figure **3** by a dashed red line. In all cases in this work, the Alfven speed for ***A*** waves is nearly identical to V_f. Within PB regions the electron density may drop several orders of magnitude below surrounding plasma values and the fast speed V_f may rise by orders of magnitude. Slow wave speeds V_s, in contrast to V_f, are relatively unaffected by such plasma bubbles, and for this reason ***S*** waves travel along magnetic field lines unimpeded by the presence of plasma bubbles.

3 Plasma Wave Observations Using Van Allen Probe Data

3.1 Van Allen Probe Observations in the Ionosphere

The pair of Van Allen Probes A and B (VAP-A and VAP-B) were launched on 30 August 2012 into highly elliptical orbits with apogee approximately 30.6 Mm, inclination approximately 18° and perigee altitudes of approximately 575 km. In the last months of the VAP mission in 2019, the perigees were lowered to approximately 275 km. Because of the high sensitivity and high sampling rate by the Van Allen probe (Mauk et al., 2013) EMFISIS (Kletzing et al., 2013) detectors, their data are most useful for plasma wave observations. One of the EMFISIS data products comprises a series of "onboard survey mode" acquisitions at 6 second intervals derived from the first 0.4681 seconds of each survey interval. These acquisitions provide the full set of magnetic (Bu, Bv, Bw) and electric (Eu, Ev, Ew) field cross spectral matrix elements, with 6 diagonal power spectral densities (PSDs) and 15 off-diagonal elements over a logarithmically distributed range of frequencies. The VAP satellites spin with a rotational period of approximately 11 seconds, and the spinning UVW coordinate system has the W axis along the spin axis, with the U and V axes perpendicular to W and to each other. The W axis is always maintained to lie within 27° of the sun's direction (Mauk et al., 2013) to keep the solar panels in the U-V plane well illuminated.

Another EMFISIS data product comprises a series of "burst mode" acquisitions, with 35 kHz sampling of all three components of the electric and magnetic fields over a period of 6 seconds. Each such burst comprises a set of 208,896 samples at a rate of 35 kHz. Contiguous bursts have a dead time gap of 0.0315 s between bursts. During the VAP mission, long (~10 minute) intervals of contiguous bursts were usually not acquired. Occasionally, as in a lightning study (Zheng et al., 2015), such burst series were acquired near perigee. In the last 10 days of the VAP mission, with perigees in the lower ionosphere, such burst series were acquired for almost every perigee passage.

It is useful to compare radar probes of ionospheric density variations with the present methods. Ground-based radar ionosonde data typically involve vertically directed, brief pulses of nearly monochromatic electromagnetic energy swept over frequencies in the MHz range. As can be seen in Figure **1a**, **1d** or **1g**, such frequencies for the ordinary **O** and extraordinary **X** waves have a strong cutoff at the plasma frequency, and radar pulses originating from ground level are reflected at the altitude where the local plasma frequency cutoff matches the radar frequency. The radar echo delay is given by the path integral of the inverse propagation speed, as in the left-hand equality of expression **11** above. As a result, the reflection time (or "virtual altitude" = the speed of light times the reflection time) as a function of radar frequency can be exploited to produce the variation of electron number density with true altitude. Similarly, in the present case, according to expression **12**, the satellite data enables a measure of the path integral of the inverse propagation speed for *each burst containing LG data* along the satellite orbit down to the relevant sub-satellite location. Ground-based soundings necessarily require a nearby radar site. Satellite-based data are not so limited.

Just as more sophisticated, phase sensitive analysis of radar data (e.g., for the determination of such observables as plasma drift speed) is possible, similar phase sensitive analysis of the satellite data is possible (Bennett, C.L. 2023), but is beyond the scope of the current article.

3.2 Scalograms of VAP data bursts

The Matlab® continuous wavelet transform (CWT) function applied to burst mode level 2 (L2) waveform data directly produces complex amplitudes over a logarithmically distributed range of frequencies. The CWT has the advantage over the more familiar fast Fourier transform (FFT) analysis, described in the following section, that higher temporal resolution information is produced for higher frequencies, while FFT analysis provides spectral information over a much coarser and fixed time-period associated with the sample used in the FFT computation. Scalogram plots in this work display the absolute value of the CWT amplitudes as a function of frequency at 28.6 μs intervals such as in Figure **5**. The L2 waveform data are calibrated in amplitude at 1kHz only and has no phase calibration applied. Since calibration factors (University of Iowa, 2022) are only available for frequencies up to 11962.89 Hz, scalogram analysis is performed using L2 waveform data without phase calibration to examine frequency components all the way to the Nyquist frequency 17.5 kHz. The quality of the agreement between the dispersion curve and the nearly dispersionless whistler at 9:16:03.389 prior to the interpolated patch in this figure demonstrates that the lack of phase calibration at the highest frequencies is unimportant.

The 0.0315 s dead time gap between successive bursts is filled in using linear interpolation between the last sample of a given burst and the first sample of an immediately succeeding burst. The representative scalogram shown in Figure **5** involves a pair of bursts concatenated with such linear interpolation. The primary artifact produced by this linear interpolation and concatenation is a suppression of high frequency components near the time of the interpolated patch of data, as best seen near the center time of the electric field scalograms in

Figure **5**. In addition, the linear interpolation can sometimes enhance low frequency components, as best seen in **5f** near the center time, where there happens to be less confusion with other low frequency structures.

3.3 Fully Calibrated Spectrograms of Contiguous Bursts of VAP data

Fully calibrated spectra for successive series of 16384 data point samples are calibrated using the FFT method and coefficients described in (University of Iowa, 2022). Each individual set of 16384 points produces a spectrum representing a 0.468 s time interval. As the number of samples in a burst divided by 16384 = 12.75, approximately every 13th spectrum in a series of consecutive bursts is affected by the linear interpolation over the 0.0315 s interval between bursts. The PSDs from contiguous data bursts are then integrated over the same series of logarithmically spaced bins as the onboard survey spectra to yield time and frequency dependent spectrograms of the mean square field values. Spectrogram plots display the mean square field values as a function of frequency at 0.468 s intervals. A representative spectrogram from a set of 100 consecutive burst acquisitions near a typical perigee pass located over the mid-Pacific Ocean is shown in Figure **6**.

3.4 Periodic Artifacts in Electric Field Data and a Mitigation Approach

A known (Kletzing et al., 2013) periodic artifact occurs when the axial boom on the side of the spacecraft pointing away from the Sun is periodically shadowed twice per spin period by the two magnetometer booms. This shadowing produces a pulse of approximately 0.3 s in the E_w component due to the sudden change in photoelectron current from the probe. In addition to this artifact, other disturbances appear at integer multiples of the spin period that primarily affect the E_w measurements. One of these artifacts manifests as brief intervals of increased scalogram intensity near $\cos(\lambda) = \pm 1$ and 0 in Figure **5f** between 3 and 30 Hz that recurs 4 times per spin period. Another artifact appears in Figure **5f** is a pair of spikes extending up to the maximum frequency located at 9:16:08.4 and 9:16:09.3 that appear once per spin period for several cycles before and after the time shown in this figure. These artifacts wax and wane over series of bursts and produce features in E_w spectra that are not true plasma wave activity. However, because of the regularity of the periodic artifacts from burst to burst over successive cycles, their temporal extent within a given burst can be estimated and avoided. Artifacts produced by interpolation can also be avoided by avoiding the dead time between bursts. Several examples of fully calibrated spectra extracted from time intervals free of such artifacts are shown in Figure **7**.

3.5 Identification and Classification of Events and Waves

As can be seen in Figures **5**, **6** and **7**, the electric and magnetic fields exhibit all forms of MHD activity. These include examples of all three modes ***F***, ***A*** and ***S*** of MHD waves. In the next two sub-sections, the ***F*** and ***S*** cases are discussed. The ***A*** mode case is represented by the spectra shown in Figure **7d** and **e**, but further discussion is beyond the scope of this article.

3.5.1 Observation of ***F*** Waves, Echoes and Plasma Bubbles in Scalograms

By virtue of the high temporal resolution of the scalograms, lightning strokes detected by the World-Wide Lightning Locator Network (WWLLN) may be unambiguously identified with events in the VAP data. WWLLN is a global Very Low Frequency (VLF; 3-30kHz) lightning location system capable of finding the radiated energy, time and location of individual lighting strokes with ~10 km spatial accuracy, ~10 μs temporal accuracy and ~90% efficiency for high peak current strokes (Abarca et al. 2010; Holzworth et al. 2019; Hutchins et al. 2012; Jacobson et al. 2006; Rodger et al. 2006). In Figure **5** three well isolated lightning strokes are seen. With the scalogram temporal resolution (28.6 μs at the highest frequencies) the accidental correlation of these whistlers with the incorrect WWLLN lightning stroke (global detection rate = 7 Hz averages 10% of the total lightning strike rate) is highly unlikely.

3.5.1.1 Echoes

As evidenced by their adherence to dispersion curves of the form $\Delta T = DC/\sqrt{f}$ in **5a-f** for the strike at 9:16:03.893 located at an angular distance of 23.5° from the sub-satellite point, ***F*** mode waves are clearly being seen. The multiple whistlers produced by this stroke have dramatically differing dispersion functions. Each dispersion curve has been delayed by the 0.01 s propagation delay through the EIWG from the stroke location to the sub-satellite point. The four more highly dispersed whistlers are identified as subprotonospheric whistlers (Chum et al., 2009) which are reflected echoes within the ionosphere as discussed earlier regarding the trapping region illustrated in Figure **4**. The curves shown have *DC* = 0.1, 12.6, 12.6*2, 12.6*3 and 12.6*4 $Hz^{1/2}$ s, consistent with dispersion constants for the echoes being proportional to the number of reflections. The simple linearity of the successive echo *DC* values suggests that the satellite altitude is not far from the lower altitude reflection location, as is consistent with the IRI model derived trapping region indicated in Figure **4d**.

Further evidence that the more highly dispersed whistlers are echoes of waves that have travelled to higher altitude and back are the “gaps” in whistler intensity starting just below Ω_H and extending almost halfway to Ω_{He} which is midway between Ω_H and Ω_O on the logarithmic scale. These gaps are best seen for the *DC* = 12.6 and 12.6*2 $Hz^{1/2}$ s whistlers in **5d** and **f**. As first pointed out by (Gurnett et al., 1965), but using De Jonghe and Keppens (2021b) nomenclature, these gaps correspond to regions where ***F*** waves have been converted to ***A*** waves by passage through plasma having a significant concentration of H^+ ions. As shown in Figure **4a**, the concentration of H^+ ions are expected to be negligible at and below the VAP altitude during the acquisition of the data shown in Figure **5**, thus indicating that the wave echoes have travelled to higher altitude with higher H^+ concentrations prior to detection. The absence of ascending frequency ***A*** wave whistlers that would normally be seen in the gaps (Gurnett et al., 1965) in Figure **5** could be attributed to their attenuation along the echoing path.

3.5.1.2 Determination of Dispersion Constants and/or Pulse Widths

A closeup of the temporal variation of the electric field components, shown both as scalograms and time resolved functions for the *DC* = 0.1 whistler from the strike at 9:16:03.893 is shown in Supplemental Figure **S2**. This figure illustrates that the (Nickolaenko et al. 2004) model for the radial electric field variations accurately predicts the propagation delay between the time of the lightning strike and the pulse arrival time at the satellite detectors. It is also clear that for dispersion constants much less than 0.1 $Hz^{1/2}$ s, the determination of *DC* from the degree of whistling in the scalograms becomes difficult. For cases below *DC* = 0.003 $Hz^{1/2}$ s, the degree of dispersion is preferably measured directly in the time domain. In the case in this supplemental figure, the *model* dispersion shown in **S2g** is characterized by the full width at half maximum (FWHM) of 0.89 s. The FWHM of the earliest peak predicted by the (Nickolaenko et al. 2004) model varies linearly with the arc-distance of propagation.

For perigee passes directly over a region of active lightning activity, a much larger number of intense ***F*** wave whistlers can be detected in the VAP data. Supplemental Figure **S3** shows an example of a single burst mode acquisition over South America in which dispersion curves for every WWLLN detected lighting stroke are plotted using $DC = 4.9\ \mathrm{Hz}^{1/2}\ \mathrm{s}$. This case illustrates that echoes may only be present for a minority of whistlers. This case also illustrates that "normal" non-echoing whistlers have only a slight variation in the dispersion constant *DC* value over a single burst of VAP data. This case also illustrates that almost every WWLLN detected lightning stroke appears as a whistler in the VAP data, but that many of the whistlers in the VAP data are not detected by the WWLLN.

3.5.1.3 Evidence for Plasma Bubbles

For each of the 100 burst datasets taken near the Mid-Pacific perigee pass exemplified by the case shown in Figure **5**, determinations of the non-echoing whistler dispersion constants have been made. These dispersion constants are plotted in Figure **6g**. Also plotted in **6g** is the IRI model dispersion constant value computed as a function of altitude from expression **12**. Clearly the altitude variation of the observed dispersion constants rather closely follows the IRI model estimate, with notable exceptional regions of extremely low and unusual dispersion. Within these regions of unusual dispersion, the magnitude of the electric field fluctuations is sometimes three orders of magnitude greater than in regions of "normal dispersion" (defined as having *DC* values approximately consistent with the IRI model estimate). The unusually strong electric field fluctuations for these extremely low dispersion events imply that at the VAP-A location the phase velocity was orders of magnitude faster than the fastest IRI model estimated phase speeds shown in Figure **4d**. The unusually low dispersion implies that the integrated plasma density along the path traversed between the source and VAP-A was orders of magnitude less than "normal". The high phase velocity, together with the unusually low dispersion suggests the presence of a plasma bubble extending over most of the path from the EIWGUB to the satellite, such as schematically illustrated in Figure **3**.

The scalograms shown in Figure **8** from the burst of data at the Eastern edge of the region of strong electric field activity seen in Figure **6d**, **e**, and **f**, (marked by the blue arrow labeled Figure **8**) corresponding to the last column of spectra in Figure **7** illustrates the transition from inside to outside a suggested plasma bubble. Inside this plasma bubble, many intense nearly dispersionless spikes appear but no normally dispersed whistlers. Outside, the intense nearly dispersionless spikes disappear and normally dispersed whistlers reappear. Near a relatively isolated nearly dispersionless spike, such as that indicated in **8f**, the time dependence of the Ew fields follows the (Nickolaenko et al., 2004) waveform. Even clearer examples of such waveforms are obtained in other perigee passes, as discussed in the following section. The observed irregular variation in the DC values on the western side of the bubble seen in Figures **3** and **6** is consistent with the structuring of the West walls of bubbles originally described by Tsunoda (1983).

3.5.1.4 A Distinctive Lightning Flash

It is apparent from the comparison between the number of nearly dispersionless spikes seen in Figure **8** that far more spikes are seen than were detected by the WWLLN. Another peculiarity is that there is poor correlation between the timing of the WWLLN spikes and the spikes observed in the three electric field components. The E_w time dependence of the strongest spike in this burst, observed near 9:17:02, has no correlated WWLLN event. Over the first second of the data in Figure **8**, for example, there are only three WWLLN events (indicated by the vertical white dashed lines extending upwards from the Oxygen cyclotron frequency) while there are numerous spikes less intense than the 9:17:02 spike but having the same shape. The number of such “extra” spikes in the electric field scalogram plots in Figure **8d**, **8e** and **8f** is clearly more than 20. The nearly dispersionless nature of these “extra” spikes manifests as the spikes extending directly vertically in the scalogram plots, without significant delay of the lower frequency portions relative to the higher frequency portions.

The Geostationary Lightning Mapper (GLM) (Bateman et al., 2020; Goodman et al., 2013; Rudlosky et al., 2019) mission is designed to provide continuous lightning measurements over most of the Western Hemisphere. A lightning flash, according to the Goodman et al., 2012, consists of “groups” of “events” located within 0.15° arc distance and no more than 330 s difference in time between the groups in a flash. During the first 9 months of GLM observations (Rudlosky et al., 2019) the mean number of groups per flash was 16.4 with a mean area of 180 km^2. The rate of GLM groups is qualitatively consistent with the number of nearly dispersionless spikes seen in Figure **8**, as well as in similar bursts of data from those cases in Figure **6g** marked as having extremely low and unusual dispersion.

Because of the high rate of nearly dispersionless spikes in such cases, it is generally difficult to connect individual spikes with specific lightning events. An exceptional case is shown in Figure **9**. The time interval marked by the broader bracket (labeled Figure **10**) corresponds to a single lightning flash observed at 9.20°N 84.75°W. Within this time interval 19 groups were detected by the GLM associated with this flash. These groups were distributed in time as shown in supplemental Figure **S4**. The supplemental figure also shows the timing and energies of the 10 WWLLN detected strokes near this location. Using the GLM clustering algorithm, all 10 of the WWLLN strokes in Figure **S4b** would be classified as originating from this single flash. For this flash, 9 of the 10 WWLLN strokes coincide in time with GLM detected groups shown in **S4c**. The single WWLLN stroke not detected by GLM was among the weakest. On the other hand, 8 of the 19 GLM groups in **S4c** were not found in the WWLLN data, including the second most intense GLM group. This flash is fortuitously timed to coincide with the passage through a hypothetical plasma bubble.

The sum of the (Nickolaenko et al. 2004) model magnetic field amplitudes from all WWLLN detected strokes is compared in Figure **10** with the ground based measured magnetic fields at the Patagonia site of the World ELF Radiolocation Array (WERA). WERA is described by Mlynarczyk et al. 2017, see also (Kulak & Mlynarczyk 2011; Kulak et al. 2012; Marchenko et al. 2022). The 10 WWLLN strokes produce 7 resolved pulses seen in Figure **10f** in the time domain and in **10e** as a scalogram. The WWLLN pulses seen in **10f** agree in relative strength ±10% with the WERA pulses seen in **10d**, although the weaker pulses are somewhat contaminated by noise in the WERA data. This validates the use of the WWLLN detected locations and energies together with the (Nickolaenko et al. 2004) model, at least for cases in which both the lighting strike and the detector are on the night side of the globe. To account for the observed dispersion in the WERA data a value of $A=(1/6-0.0073i)/2\pi$ in the notation of (Nickolaenko et al. 2004) was used. The arrival times of the model pulses in **10f** appear to be consistently later by 1 ms than the WERA observed pulses, corresponding to a observed propagation speed through the EIWG of 255 Mm/s over the 63° arc-distance from flash to detectors.

For the 0.3 s interval in Figure **11** three WWLLN detected lightning strokes were detected, and just as in prior scalogram plots, the dispersion curves for the three WWLLN whistlers are shown by the red curved dashed lines superimposed on the scalograms. Dispersion curves for the four pulses at the GLM times are indicated by the white dashed lines. Using the WWLLN measured energy for these strokes, with the assumption that all this energy is conveyed to the Q-bursts diverging away from the location of each stroke, the (Nickolaenko et al., 2004) Q-burst radial electric field is shown in Figure **11g**. As the VAP spin axis is most closely aligned with the vertical direction, the model time dependence of **11g** is best compared with the observed electric field variation in **11f**. In contrast to the case for normally dispersed whistlers, there is a substantial discrepancy between the WWLLN/GLM derived arrival times, and the VAP observed arrival times as indicated in **11e**. The relative amplitudes of the three WWLLN detected pulses in **11f** to the model pulse amplitudes in **11g** exhibit a correlation with the propagation delay. The greater the delay, the greater the attenuation relative to the model. However, even the most delayed pulses have no discernable extra dispersion beyond that already accounted for by the (Nickolaenko et al., 2004) model with the value of $A=(1/6-0.0073i)/2\pi$ used to fit the width of the pulses in the WERA magnetic field data.

3.5.1.5 Are the Roots of Plasma Bubbles Foamy?

The apparent strong variation in both the propagation delay and pulse attenuation, but without significant additional dispersion for the Q-bursts passing through plasma bubbles described above suggests that the plasma bubbles may have a micro-structure analogous to that of foamy liquids. Such foamy materials exhibit significant variations in both acoustic wave velocity and attenuation with composition, as described by Pierre et al. (2013) for example, but without significant dispersion as a function of frequency. Here the appellation “foamy” is meant to apply to regions of size no smaller than the minimum wavelength associated with ***F*** wave propagation through “normal” plasma but containing numerous embedded field aligned bubbles. A more detailed examination of this hypothesis is given in (Bennett, C.L., 2023).

3.5.2 Observation of ***S*** waves in Magnetic Field Scalograms

In contrast to the electric field scalograms, the magnetic field fluctuations are generally much less dynamic and much more systematic in the ionosphere. The scalograms in Figure **5** show that the B_u and B_v fluctuations have components with clear periodic behavior that are 90° out of phase with each other. The VAP spin period during these data is 10.76 s and is identical with the B_u and B_v fluctuation period seen directly in their variations in **5a** and **b**. Similar variations correlated with the spin angle are seen in Figures **8** & **9**. The clear periodicity and 90° phase difference in the B_u and B_v fluctuations can also be seen in Figure **6a** and **b**, as well as their “insensitivity” to the substantial variations in the electric field variations.

These fluctuations at the VAP spin period in the magnetic scalograms of Figure **5a** & **b** are identified as ***S*** waves based on their speed. The upper limit on the speed of these waves derived from periods not having significant ***F*** wave activity such as in Figure **7c** and **7i** is so much less than $V_f = 609$ km/s for a primarily O^+ plasma (cf. Figure **1f**) that they can only be from ***S*** waves. Although *emitted* frequencies for V_s waves in an O^+ plasma do not extend above Ω_O, the large *DFR* factors of **expression 6** for $V_o/V_g = 9.6/1.4$ “kick” the *observed* frequencies far above Ω_O and could plausibly produce the $1/f^2$ spectral variation generally seen in the B_u and B_v spectra in Figure **7a**, **d**, **g** and **j** extending to a white noise floor at high frequency. The ***S*** mode assignment for these waves is further confirmed by their angular distribution. The absence of B_u activity near cos(λ)=±1 in **5a**, when the U axis is aligned with $\widehat{\boldsymbol{B}}_{\mathbf{0}}$, and the absence of B_v activity near cos(λ)=0 in **5b** when the V axis is aligned with $\widehat{\boldsymbol{B}}_{\mathbf{0}}$, is clear in these plots. As seen in **2c**, low frequency ***S*** wavevectors become insignificant in directions perpendicular to $\widehat{\boldsymbol{B}}_{\mathbf{0}}$, so that ***S*** wave magnetic field fluctuations (that must be perpendicular to $\widehat{\boldsymbol{k}}$) become insignificant in directions parallel to $\widehat{\boldsymbol{B}}_{\mathbf{0}}$. The EMFISIS magnetic field fluctuation noise floor can be assessed from the intervals near the absence of ***S*** wave activity in the B_u data near cos(λ)=±1 in **5a** or in the B_v data near cos(λ)=0 in **5b**. In these intervals, the EMFISIS B field noise floor is found to be below 0.1 pT for frequencies between 3 and Ω_H.

The large doppler shift effects on the ***S*** wave activity precludes the possibility of observing possible resonance peaks in the VAP magnetic field spectra. However, the dependence of the doppler shifts on the orbital inclination suggests that magnetic field data from satellites in low earth *polar* orbits might be better suited for analysis of the spectral content of ***S*** wave activity. High-rate Swarm magnetic field data are particularly useful in this regard as discussed in section 4 below.

3.6 Systematics of ***S*** Wave Variations

The characteristic ***S*** wave activity seen in Figure **5a** & **b** is seen throughout the VAP mission and throughout the ionosphere. Figure **12** showing the electric and magnetic field survey mode PSDs averaged over altitudes less than 1 Mm makes this clear. The intensity of this activity has clear correlation with geodetic location, as shown in Figure **13**. In this figure, the rms magnetic field fluctuations were computed from the calibrated spectra for every set of consecutive 16,384 samples available from perigee crossings during the last 10 days of the VAP mission. Altogether a total of 26,892 such rms values were available. The average rms values within 10 km wide altitude bins, 30° wide longitude bins, and 1° wide magnetic latitude bins were computed for the plots shown. The peak seen in Figure **13** near 90°E, 15°S corresponds to a local maximum (Cecil et al., 2014) in the lightning rate, as expected for LG ***S*** waves. The systematic decrease of the intensity with altitude is consistent with these waves being generated below the satellite and experiencing some degree of attenuation as they propagate upwards.

4 Swarm Satellite Observations of Plasma Waves in the Ionosphere

The Swarm constellation of three nominally identical satellites: Alpha, Bravo and Charlie, (SwA, SwB and SwC) packed into a single bus were launched into a near polar orbit on 22 November 2013. By mid-March 2014, SwB was raised to its design altitude of approximately 525 km. The core instrument of the Swarm mission (Olsen et al., 2013) is the Vector Field Magnetometer (VFM). The VFM is a triaxial fluxgate magnetometer (Merayo, 2014; Primdahl & Jensen, 1981), consisting of three concentric spherical coils having mutually perpendicular axes. Three orthogonal sensor core coils within the spherical coils are provided to measure the three components of the magnetic field in directions determined by the coil orientation and highly insensitive to possible misalignments of the sensor coils. The sample rate of the VFM data is 50 Hz, thus a Nyquist frequency of 25 Hz. This frequency range of magnetic field fluctuations is especially well suited for the detection of ***S*** wave activity. The computations of scalograms and spectrograms from these data are performed as described above for the Van Allen Probe data.

For the first couple of months of the Swarm mission, SwA, B & C had a "beads on a string" orbital geometry, following each other very closely in space & time. During this phase, the spacing between the satellites gradually increased. Over the course of the next few months, SwA was lowered to its working altitude, SwB was raised to its working altitude and SwC was lowered to its working altitude. The orbital changes during this initial phase of the Swarm mission are indicated in supplemental Figure **S5**.

At 21:01:30 on 14 March 2014 two days after SwB was raised to its operational altitude of 525 km, a mysterious chirping in the high rate SwB VFM-y channel data as seen in Figure **14b** suddenly appeared. Exactly at the time that this chirping appeared, the overall noise level also suddenly increased *in the y channel*, as can be seen in the spectrograms. Near the time of this change in the y channel data, there was no similar change in either the x or z VFM channels. A systematic diurnal variation in the noise level in the x channel was seen, with greater noise in the afternoon and less noise in the pre-dawn. The overall increased SwB y channel noise level was not significantly different between the dayside and nightside of the orbits and did not depend on longitude. The mysterious chirping is found to be correlated with the alignment of the SwB velocity vector to the ambient magnetic field direction, as can be seen by comparison of Figure **14** sections **b** and **d** in this and in each of the similar figures shown in the supplemental materials.

This chirping just as suddenly ceased at 11:17:53 on 25 June 2014 as shown in supplemental Figure **S6**. The cessation of chirping coincided with a manual power cycling of the VFM instrument on SwB. According to (European Space Research and Technology Centre, 2018), at the time that the chirping disappeared from the data, it is stated "70pT noise in y-measurement since [14 March 2014]". After this power cycling, the overall background noise level in the y channel returned to that seen before the onset of chirping shown in Figure **14**. The overall background noise levels in the x and z channels did not significantly change after the power cycle.

Between 5:50 on 8 May 2014 and 7:20 on 9 May 2014, a series of four 90° yaw slew maneuvers of the SwB satellite were conducted and after each of the 90° yaw slews the observed chirping ***apparently*** transforms back and forth between the East-West and North-South directions. Throughout the entire time the chirping is observed, however, it is confined to the single VFM-y channel. Data from the interval around the first yaw slew are shown in Figure **S7**. During the slew process the various resonant frequencies are disturbed. After the slew completes, the character of the resonance variations matches the character before the slew began. Very similar variations happen for the subsequent three slew maneuvers.

It is suggested here that the unusual SwB VFM-y signals are not instrumental artifacts, but rather signals produced by doppler shifted resonances. In support of this, the centroid of the distribution of doppler shifted frequencies using **expression 7** for the lowest Schumann resonance frequency of 7.8 Hz is plotted with the assumption of a *fixed* value for the ratio of V_o/V_g. With the SwB speed being 7.6 km/s, and with a speed for H^+ plasma waves at the 525 km SwB altitude of approximately 5 km/s, as shown in Figure **4** for example, V_o/V_g is approximately 1.5, but without detailed measurements of the ionospheric composition and temperature, this is only an estimate. Even so, the strongest of the resonance features seen in Figure **14** qualitatively follows the behavior of the doppler shifted frequency variation. Note, for example, that the observed frequency of this resonance in **14b** appears to pass through zero, reaching a minimum negative value near 21:40, but because the measured frequencies are restricted to positive values between 0 and 25 Hz, the would be negative "valley" appears as a positive peak. Also, at times that the spacecraft passes over the magnetic poles, where the local magnetic field is vertical, such as at the times 22:05, 22:52 and 23:40, according to **expression 7**, the centroid of the doppler shift distribution is unshifted and the width of the distribution becomes maximal.

Surrounding the crossing of the magnetic poles, upon passage through the auroral regions as described by (McGranaghan et al., 2017), field aligned currents (FACs) produce significant fluctuations in the magnetic fields. These disturbances are seen in all VFM components, but there is a region inside the auroral oval where the FAC disturbance is not so dominant, and the appearance of the unshifted, but broadened fundamental Schumann resonance frequency becomes apparent. Among the polar crossings in Figure **14**, the case at 22:05 shows the clearest evidence for the lowest SR frequency with the case at 23:40 displaying similar behavior. In the supplemental Figure **S6**, at 8:06 a particularly clean auroral oval center region shows the lowest SR frequency *quantitatively* following the simple doppler shift model. It can generally be seen that the resonances indeed appear broader near the poles than near the equator, as predicted by expression **7**.

There are several resonance features in the SwB VFM-y channel data beyond the SR fundamental. Without more accurate knowledge of the ionospheric composition, its temperature and possible bulk plasma drift velocities, it is not feasible to precisely model these features, such as the higher SR resonances or other possible ionospheric resonances. Finally, a more subtle feature of the chirping in the data is that each of the resonance features appears to have a fainter "echo" at exactly 25 Hz minus the frequency of the resonance. This is clearest in **14b** near 21:00, for example, but this echo is present throughout Figure **14**, and supplemental figures **S6** and **S7**. It is suspected that these echoes are indeed instrumental artifacts.

Less direct evidence in support of the reality of the existence of the resonances in the SwB data is that the rms magnetic field fluctuations seen in the SwB VFM-y channel data during the time that the mysterious resonances are seen are typically between 0.1 and 0.2 nT. This value is consistent with the magnetic field fluctuations measured at the SwB altitude with the VAP, as shown in Figure **13**. On the other hand, for the other VFM channels, and for the other Swarm satellites, the magnetic field noise level is much less, and is NOT consistent with the expectations from the far more sensitive EMFISIS data. It appears that for most of the Swarm mission, there was apparently an effective low pass filter involved in the data processing that precludes the ability to measure the resonances described here.

Further evidence for an apparent low pass filter afflicting most of the Swarm mission is the presence of the chirping seen in the CHAMP data (that presumably did not have a similar low pass filter) and discussed by Yin et al. (2015). The W-shaped features these authors show in their Figure **12**, for example, have the same shape as the model shown here in Figure **14d** for the 7.8 Hz fundamental Schumann Resonance frequency. Quantitatively, even the magnitude of the peak value of the center of the W-shape can be reproduced by slightly raising the V_o/V_g parameter. The explanation given for these chirp features by Yin et al. (2015) was that they were produced as the B_y component of the magnetic field passed through zero. This explanation does not work for the SwB data. The VFM_y measurements do not pass through zero at the time the W-shapes are present, as seen in Figure **14e**.

Finally, the most compelling evidence for the presence of a low pass filter in the Swarm VFM archived data is provided by the clear observation of strong whistler events in the Swarm

Absolute Scalar Magnetometer (ASM) data that *SHOULD* also be seen in the VFM data but are missing. On the website (Coisson, 2022) an example of a strong whistler seen in ASM data from the SwB satellite at 11:30:57 on 19 Jan 2014 is shown. The scalograms derived from the SwB VFM data for a four-hour period including the time of this whistler is shown in supplemental Figure **S8**. Despite the proven existence of the whistler in the ASM data at a level well above 100 pT^2/Hz, nothing above the VFM background level ~1 pT^2/Hz appears in the VFM data at the same time. Apparently, for some unknown reason, the low pass filter on the single VFM-y channel data on the single SwB satellite was not in effect for the period of the mysterious chirping.

5 Conclusions

Evidence for a persistent population of slow magnetosonic waves in the ionosphere has been presented. Evidence for the presence of a small number of resonances in these waves has also been found. The intensity of the electric field disturbances seen in the Van Allen probe data near suggested plasma bubbles are consistent with the intensities of (Ni & Zhao, 2005). The intensity of the magnetic field resonances seen in Swarm Bravo data is also consistent with their results. The strong dependence on doppler shift effects on the inclination of satellite orbits can explain differences between Van Allen probe and Swarm observations of low-speed magnetic field plasma waves. Although the point that the magnetic field resonances seen here in the Swarm data and by Ni & Zhao cannot be simple leakage of magnetic Schumann Resonances from the Earth ionosphere waveguide (EIWG) is well taken since they are so strong, this does not prove that these waves could not have been produced by the conversion of electric field oscillations to slow magnetosonic waves in the complex interaction region of the EIWG upper boundary (EIWGUB). In the EIWGUB region with a strongly increasing value of β with altitude as seen in Figure **4e**, according to (Akhtar et al., 2021) collisional effects could play a significant role in converting LG energy in the EIWG to slow magnetosonic waves able to propagate upwards into the ionosphere. Since LG energy in the EIWG is ubiquitous and omnipresent, such a conversion process could lead to ubiquitous and omnipresent slow magnetosonic waves in the ionosphere.

If the suggestions of this work are accepted, some of the discrepancy between model and along-track magnetic field difference observations tabulated by (Finlay et al., 2020) could perhaps be produced by these waves. Better knowledge of these hitherto unremarked plasma structures in the ionosphere could perhaps help better understand and interpret past and future satellite measurements of the earth's magnetic field and ionospheric plasma wave activity.

For satellites at the low altitude, as for the perigees during the last eight months of the Van Allen probe mission, the discussion above illustrates a new method for the investigation of plasma bubble structure. As roughly half of the Van Allen perigees passed through plasma bubbles, based on inspection of data such as shown in Figure **6**, much more analysis of the roots of plasma bubbles remains to be explored.

Finally, if the suggestions of this work are accepted that a low pass filter is present in the analysis chain of high rate VFM Swarm data and if it is possible to remove this filter, a new tool for the investigation of slow magnetosonic waves in the ionosphere may become available for the remainder of the Swarm satellite mission.

Acknowledgments

The work of the EMFISIS team in the production of Van Allen probe data is gratefully acknowledged. WERA data used in this paper was provided by Jerzy Kubisz of the Astronomical Observatory of the Jagiellonian University, and the author thanks him and the WERA project personnel for their help in understanding this data. The author thanks Jordi De Jonghe for helpful discussion, especially regarding dispersionless wave propagation analysis.

Open Research

Van Allen Probe data used in this paper can be found in the EMFISIS archive (http://emfisis.physics.uiowa.edu/data/index). In this index file, descriptions of each of the relevant data sets, including the file naming format, are provided. The specific level 2 data products involved in the present work include the "WFR-waveform-continuous-burst_emfisis-L2", "WFR-spectral-matrix-diagonal_emfisis-L2", "magnetometer_uvw_emfisis-L2". The specific level 3 data products are "magnetometer_hires-geo_emfisis-L3". Swarm data used in this paper is provided by the European Space Agency and can be accessed online at https://swarm-diss.eo.esa.int. The high rate VFM data was taken from the level 1b "latest_baselines" folder containing "MACx_HR" files for each of the three Swarm satellites. WERA data used in this paper is described in detail on the WERA project website: http://www.oa.uj.edu.pl/elf/index/projects3.htm and may be freely available for scientific analysis by contacting the WERA personnel. WWLLN data was purchased from the University of Washington (https://wwlln.net). GLM data is available at no cost from the Geostationary Operational Environmental Satellites-R Series web site (https://www.goes-r.gov), but the user must register to obtain the GOES-R Series GLM L2+ Data Product "GRGLMPROD" and must select an appropriate time range for data access on the web-page: https://www.avl.class.noaa.gov/saa/products/search?datatype_family=GRGLMPROD.

References

Abarca, S.F., Corbosiero, K.L., & Galarneau Jr., T.J. (2010). An evaluation of the Worldwide Lightning Location Network (WWLLN) using the National Lightning Detection Network (NLDN) as ground truth. Journal of Geophysical Research, 115(D18206). https://doi.org/10.1029/2009JD013411

Abdu, M.A., Batista, I.S., Reinisch, B.W., MacDougall, J.W., Kherani, E.A., & Sobral, H.H.A (2012). Equatorial range spread F echoes from coherent backscatter, and irregularity growth processes, from conjugate point digital ionograms., *Radio Science*, 47, RS6003. https://doi.org/10.1029/2012RS005002

Abdu, M.A., Muralikrishna, P., Batista, I.S., Sobral, J.H.A. (1991). Rocket observation of equatorial plasma bubbles over Natal, Brazil, using a high-frequency capacitance probe. *Journal of Geophysical Research: Space Physics, 96*(A5), 7689-7695. https://doi.org/10.1029/90jA02384

Adkins, V.J. & England, S.L. (2022). *Automated detection, tracking, and analysis of nightside ionospheric instabilities from 2018 to 2022 in 135.6 nm airglow data from the Global-Scale Observations of the Limb and Disk (GOLD) Mission*. Poster presented at AGU fall meeting, Chicago, Illinois, USA.

Akhtar, N, Hussain, S., & Mahmood, S. (2021). Nonlinear propagation of fast and slow magnetosonic waves in collisional plasmas. *Contributions to Plasma Physics*. https://doi.org/10.1002/ctpp.202000210

Alken, P., Thebault, E., Beggan, C.D., Amit, H., Aubert, J., Baerenzung, J., et al. (2021). International Geomagnetic Reference Field: the thirteenth generation. *Earth, Planets and Space 73,* 49. https://doi.org/10.1186/s40623-020-01288-x

Bateman, M., Mach, D., & Stock, M. (2020). Further investigation into detection efficiency and false alarm rate for the geostationary lightning mappers aboard GOES-16 and GOES-17. *Earth and Space Science, 8*, 2020EA001237. https://doi.org/2020EA001237

Bennett, C.L. (2023). Observations of the Roots of Plasma Bubbles: Are they sometimes foamy? *Authorea*. March 9, 2023, doi:10.22541/essoar.167839960.01635070/v1

Bilitza, D., Altadill, D., Truhlik, V., Shubin, V., Galkin, I., Reinisch, B. & Huang, X. (2016). International Reference Ionosphere 2016: From ionospheric climate to real-time weather predications. *Space Weather*, *15*, 418-429. https://doi.org/10.1002/2016SW001593

Boldi, R., Williams, E. & Guha, A. (2017). Determination of the Global-Averal Charge Moment of a Lightning Flash Using Schumann Resonances and the LIS/OTD Lightning Data. *JGR: Atmospheres, 123,* 108-123. https://doi.org/10.1002/2017JD027050

Budden, K.G. (1957). The “wave-guide” Mode Theory of the Propagation of Very-Low-Frequency Radio Waves. *Proceedings of the IRE 45,* 772-774. https://doi.org/10.1109/JRPROC.1957.278471

Burgesser, R.E. (2017). Assessment of the World Wide Lightning Location Network (WWLLN) detection efficiency by comparison to the Lightning Imaging Sensor (LIS). *Quarterly Journal of the Royal Meteorological Society, 143,* 2809-2817. https://doi.org/10.1002/qj.3129

Cecil, D. J., Buechler, D.E. & Blakeslee, R.J. (2014). Gridded lightning climatology from TRMM-LIS and OTD: Dataset description. *Atmospheric Research, 135-136,* 404-414. https://doi.org/10.1016/j.atmosres.2012.06.028

Chapman, F.W, Llanwyn Jones, D., Todd, J.D.W., & Challinor, R.A. (1966). Observation on the propagation constant of the Earth-ionosphere waveguide in the frequency band 8 c/s to 16 kc/s. *Radio Science,1,* 1273-1282. https://doi.org/10.1002/rds19661111273

Chen, L. & Thorne, R. (2012). Perpendicular propagation of magnetosonic waves. *Geophysical Research Letters, 39*(14), L14102. https://doi.org/10.1029/2012GL052485

Chum, J., Santolik, O. & Parrot, M. (2009). Analysis of subprotonospheric whistlers observed by DEMETER-A case study. *Journal of Geophysical Research: Space Physics, 114,* A02307. https://doi.org/10.1029/2008JA013585

Coisson, P. (2022). Investigating Lightning Generated ELF Whistlers to Improve Ionospheric Models (ILGEW) website: https://ilgew.ipgp.fr/#presentation

Crisp, N.H., Roberts, P.C.E., Livadiotti, S., Oiko, V.T.A. Edmondson, S., Haigh, S.J., et al. (2020). The benefits of very low earth orbit for Earth observation missions. *Progress in Aerospace Sciences, 117*(August 2020, 100619). https://doi.org/10.1016/j.paerosci.2020.100619

De Jonghe, J. & Keppens, R. (2020a). A two-fluid analysis of waves in a warm ion-electron plasma. *Plys. Plasmas*. *27*, 122107. https://doi.org/10.1063/5.0029534

De Jonghe, J. & Keppens, R. (2020b). Two-Fluid Treatment of Whistling Behavior and the Warm Appleton-Hartree Extension. *Journal of Geophysical Research: Space Physics, 126,* e2020JA028953. https://doi.org/10.1029/2020JA028953

European Space Research and Technology Centre. (2018, 3 31). *Swarm Spacecraft Anomalies and Manoeuvres History (till 31 March 2018).* Retrieved from https://earth.esa.int/eogateway/documents/20142/37627/Swarm_manoeuvres.pdf/5e7ccf65-67ec-2d1a-6e65-d6d4bd7ee032

Finlay, C.C., Kloss, C., Olsen, N., Hammer, M.D., Toffner-Clausen, L., Grayver, A. & Kuvshinov, A. (2020). The CHAOS-7 geomagnetic field model and observed changes in the South Atlantic Anomaly. *Earth, Planets and Space, 72*(156), 1-31. https://doi.org/10.1186/s40623-020-01252-9

Friis-Christensen, E., Luhr, H. & Hulot, G. (2006). Swarm: a constellation to study the Earth's magnetic field. *Earth Planets and Space, 58*(4)*,* 351-358. https://doi.org/10.1186/BF03351933

Fullekrug, M. (1995). Schumann resonances in magnetic field components. *Journal of Atmospheric and Terrestrial Physics, 57*(5), 479-484. https://doi.org/10.1016/0021-9169(94)00075-Y

Fullekrug, M. & Fraser-Smith, A.C. (1996). Further evidence for a global correlation of the Earth-ionosphere cavity resonances. *Geophysical Research Letters, 23*(20), 2773-2776. https://doi.org/10.1029/96GL02612

Goedbloed, H., Keppens, R. & Poedts, S. (2019). *Magnetohydrodynamics of Laboratory and Astrophysical Plasmas.* Cambridge, United Kingdom: Cambridge University Press.

Goodman, S., Blakeslee, R., Koshak, W., Mach, D., Bailey, J., Buechler, D., et al. (2013). The goes-r Geostationary Lightning Mapper (GLM). *Atmospheric Research, 125-126*, 34-49. https://doi.org/10.1016/j.atmosres.2013.01.006

Goodman, S., Mach, D., Koshak, W., Blakeslee, R. (2012). Algorithm theoretical basis document: GLM lightning cluster-filter algorithm. Version 3.0. July 30, 2012. NOAA NESDIS Center for satellite applications research.

Gurnett, D.A., Shawhan, S.D., Brice, N.M. & Smith, R.L. (1965, April 1). Ion Cyclotron Whistlers. *Journal of Geophysical Research, 70*(7), 1665-1688.

Holzworth, R.H., McCarthy, M.P., Brundell, J.B., Jacobson, A.R. & Rodger, C.J. (2019). Global Distribution of Superbolts. *Journal of Geophysical Research: Atmospheres, 124*(17-18), 9996-10005. https://doi.org/10.1029/2019JD030975

Hutchins, M.L., Holzworth, R.H., Rodger, C.J., & Brundell, J.B. (2012). Far-field power of lightning strokes as measured by the world-wide lightning location network. *Journal of Atmospheric and Oceanic Technology, 29*, 1102-1110. https://doi.org/10.1175/JTECH-D-11-00174.1

Hysell, D.L., Larsen, M.F., Swenson, C.M., Barjatya, A., Wheeler, T.F., Sarango, M.F., et al. (2005). Onset conditions for equatorial spread F determined during EQUIS II. *Geophysical Research Letters*, *32* (L24104). https://doi.org/10.1029/2005GL024743

Immel, T.J., Mende, S.B., Frey, H.U., Peticolas, L.M., & Sagawa, E. (2003). Determination of low latitude plasma drifts speeds from FUV images. *Geophysical Research Letters, 30*(18), 1945. https://doi.org/10.1029/2003GL017573

Jackson, J.D. (1975). *Classical Electrodynamics.* New York: John Wiley & Sons.

Jacobson, A.R., Holzworth, R., Harlin, J., Dowden, R. & Lay, E. (2006). Performance Assessment of the World Wide Lightning Location Network (WWLLN), Using the Los Alamos Sferic Array (LASA) as Ground Truth. *Journal of Atmospheric and Oceanic Technology, 23*(8), 1082-1092. https://doi.org/10.1175/JTECH1902.1

Jacobson, A.R., Holzworth, R.H., Pfaff, R.F. & McCarthy, M.P. (2011). Study of oblique whistlers in the low-latitude ionosphere, jointly with the C/NOFS satellite and the World-Wide Lightning Location Network. *Annales of Geophyics, 29*(5), 851-863. https://doi.org/10.5194/angeo-29-851-2011

Karan, D.K., Daniell, R.E., England, S.L., Martinis, C.R., Eastes, R.W., Burns, A.G., & McClintock, W.E. (2020). First zonal drift velocity measurement of equatorial plasma bubbles (EPBs) from a geostationary orbit using GOLD data. *Journal of Geophysics: Space Physics 125*, e2020JA028173. https://doi.org/10.1029/2020JA028173

Kil, H., Demajistre, R., & Paxton, L.J. (2004). F-region plasma distribution seen from TIMED/GUVI and its relation to the equatorial spread F activity. *Journal of Geophysical Research, 31*, L05810. https://doi.org/10.1029/2003GL018703

Kletzing, C.A., Kurth, W.S., Acuna, M., MacDowall, R.J., Torbert, R.B., Averkamp, T., et al. (2013). The Electric and Magnetic Field Instrument Suite and Integrated Science (EMFISIS) on RBSP. *Space Science Reviews, 179,* 127-181. https://doi.org/10.1007/s11214-013-9993-6

Kudeki, E., & Bhattacharyya, S. (1999). Postsunset vortex in equatorial F-region plasma drifts and implications for bottomside spread F. *Journal of Geophysical Research*, 104(A12), 28, 163-28, 170. https://doi.org/10.1029/1998JA900111

Kulak, A. & Mlynarczyk, J. (2011). A new technique for reconstruction of the current moment waveform related to a gigantic jet from the magnetic field component recorded by an ELF station. *Radio Science, 46*, RS2016. https://doi.org/10.1029/2010RS004475

Kulak, A., Mlynarczyk, J., Ostrowski, M., Kubisz, J., & Michalec, A. (2012). Analysis of ELF electromagnetic field pulses recorded by the Hylaty station coinciding with terrestrial gamma-ray flashes. *Journal of Geophysical Research, 117*, D18203. https://doi.org/10.1029/2012JD018205

Makela, J.J., & Kelley, M.C. (2003). Field-aligned 777.4-nm composite airglow images of equatorial plasma depletions. *Geophysical Research Letters, 30*(8), 1442. https://doi.org/10.1029/2003GL017106

Marchenko, V., Kulak, A., & Mlynarczyk, J. (2022). Finite-difference time-domain analysis of ELF radio wave propagation in the spherical Earth-ionosphere waveguide and its validation based on analytical solutions. *Annales of Geophysics, 40*, 395-406. https://doi.org/10.5194/angeo-40-395-2022

Martinis, C., Eccles, J.V., Baumgardner, J., Manzano, J., & Mendillo, M. (2003). Latitude dependence of zonal plasma drifts obtained from dual-site airglow observations. *Journal of Geophysical Research, 108*(A3), 1129. https://doi.org/10.1029/2002JA009462

Mauk, B.H., Fox, N.J., Kanekal, S.G., Kessel, R.L., Sibeck, D.G., & Ukhorskiy, A. (2013). Science Objectives and Rationale for the Radiation Belt Storm Probes Mission. *Space Sci Rev. 179,* 3-27. https://doi.org/10.1007/s11214-012-9908-y

McGranaghan, R.M, Mannucci, A.J. & Forsyth, C. (2017). A Comprehensive Analysis of Multiscale Field-Aligned Currents: Characteristics, Controlling Parameters, and Relationships. *Journal of Geophysical Research: Space Physics 122*(12), 11,931-11,960. https://doi.org/10.1002/2017JA024742

Mendillo, M., & Baumgardner, J. (1982). Airglow characteristics of equatorial plasma depletions. *Journal of Geophysical Research, 87*(A9), 7641-7652. https://doi.org/10.1029/JA087iA09p07641

Merayo, J.M.G. (2014, June 19-20). The Swarm Vector Field Magnetometer (VFM): instrument comissioning and performance assessment. *3rd Swarm Science Meeting* (pp. 1-18). Copenhagen, Denmark: DTU Space National Space Institute.

Mlynarczyk, J., Kulak, A., & Salvador, J. (2017). The accuracy of radio direction finding in the extremely low frequency range. Radio Science, 52, 1245-1252. https://doi.org/10.1002/2017RS006370

Narayanan, V.L., Sau, S., Gurubaran, S., Shiokawa, K., Balan, N., & Emperumal, K. (2014). A statistical study of satellite traces and subsequent evolution of equatorial spread F based on ionosonde observations over dip equatorial site Tirunelveli, India. *Earth, Planets and Space*, 676(1), 160. https://doi.org/10.1186/s40623-014-0160-4

Ni, B.B. & Zhao, Z.Y. (2005). Spatial Observations of Schumann Resonace at the Ionospheric Altitudes. *Chinese Journal of Geophysics, 48*(4), 818-826. https://doi.org/10.1002/cjg2.719

Nickolaenko, A.P. & Hayakawa, M. (2002). *Resonances in the Earth-Ionosphere Cavity.* Dordrecht/Boston/London: Kluwer Academic Publishers.

Nickolaenko, A.P., Hayakawa, M., T. Ogawa & Komatsu, M. (2008). Q-bursts: A comparison of experimental and computed ELF waveforms. *Radio Science, 43*(RS4014), 1-9. https://doi.org/10.1029/2008RS003838

Nickolaenko, A.P., Rabinowicz, L.M. & Hayakawa, M. (2004). Time domain presentation for ELF pulses with accelerated convergence. *Geophysical Research Letters, 31*(L05808), 1-4. https://doi.org/10.1029/2003GL018700

Ogawa, T., Tanaka, Y., Yasuhara, M., Fraser-Smith, A.C. & Gendrin, R. (1967). Worldwide Simultaneity of Occurrence of a Q-type ELF Burst in the Schumann Resonance Frequency Range. *Journal of Geomagnetism and Geoelectricity, 19*(4), 377-384. https://doi.org/10.5636/jgg.19.377

Olsen, N., Friis-Christensen, E., Floberghagen, R., Alken, P., Beggan, C., Chulliat, A., et al. (2013). The Swarm Satellite Constellation Application and Research Facility (SCARF) and Swarm data products. *Earth Planets Space 65*(1), 1189-1200. https://doi.org/10.5047/eps.2013.07.001

Patra, A.K., Yokoyama, T., Yamamoto, M., Saito, S., Maruyama, T. & Fukao, S. (2005). Disruption of E region echoes observed by the EAR during the development phase of equatorial spread F: A manifestation of electrostatic field coupling. *Geophysical Research Letters, 32*(L17104). https://doi.org/10.29/2005GL022868

Pierre, J., Guillermic, R., Elias, R., Drenckhan, W., & Leroy, V. (2013). Acoustic characterization of liquid foams with an impedance tube. *The European Physical Journal E 36*(113). https://doi.org/10.1140/epje/i2013-13113-1

Pimenta, A.A., Bittencourt, J.A., Fagundes, P.R., Sahai, Y., Buriti, R.A., Takahashi, H., & Taylor, M.J. (2003). Ionospheric plasma bubble zonal drifts over the tropical region: A study using OI 630 nm emission all-sky images. *Journal of Atmospheric and Solar-Terrestrial Physics, 65*(10), 1117-1126. https://doi.org/10.1016/S1364-6826(03)00149-4

Price, C. (2016). ELF Electromagnetic Waves from Lightning: The Schumann Resonances. *Atmosphere 7*(9), 116. https://doi.org/10.3390/atmos7090116

Primdahl, F. & Jensen, P.A. (1981). Compact spherical coil for fluxgate magnetometer vector feedback. *J. Phys. E: Sci. Instrum. 15*(2) . https://doi.org/10.1088/0022-3735/15/2/015

Rodger, C.J., Werner, S., Brundell, J.B., Lay, E.H., Thomson, N.R., Holzworth, R.H. & Dowden, R.L. (2006). Detection efficiency of the VLF World-Wide Lightning Location Network (WWLLN): initial case study, *Annales of Geophysics, 24*, 3197-3214. https://doi.org/10.5194/angeo-24-3197-2006

Rodriguez-Camacho J., Salinas, A., Carrion, M.C., Porti, J., Fornieles-Callejon, J. & Toledo-Redondo, S. (2021). Four Year Study of the Schumann Resonance Regular Variations Using the Sierra Nevada Station Ground-Based Magnetometers. *Journal of Geophysical Research: Atmospheres, 127*(6) e2021JD036051. https://doi.org/10.1029/2021JD036051

Rodriguez-Zuluaga, J., Stolle, C., Hysell, D. & Knudsen, D.J. (2022). Topside equatorial spread F-related field-aligned Poynting flux: observations and simulations. *Earth, Planets and Space, 74*(119). https://doi.org/10.1186/s40623-022-01679-2

Rodriguez-Zuluaga, J., Stolle, C., Yamazaki, Y., Xiong, C., & England, S.L. (2020). A synoptic-scale wavelike structure in the nighttime equatorial ionization anomaly. *Earth and Space Science, 8*, e2020EA001529. https://doi.org/10.1029/2020EA001529

Rudlosky, S., Goodman, S., Virts, K., & Bruning, E. (2019). Initial Geostationary Lightning Mapper observations. *Geophysical Research Letters, 46*, 1097-1104. https://doi.org/10.1029/2018GL081052

Salinas, A., Toledo-Redondo, S., Navarro, E.A., Fornieles-Callejon, J. & Porti, J.A. (2016). Solar storm effects during Saint Patrick's Days in 2013 and 2015 on the Schumann resonances measured by the ELF station at Sierra Nevada (Spain). *Journal of Geophysical Research: Space Physics, 121*(12) 12,234-12,246. https://doi.org/10.1002/2016JA023253

Santolik, O., Parrot, M., Inan, U.S., Buresova, D., Gurnett, D.A. & Chum, J. (2009). Propagation of unducted whistlers from their source lightning: A case study. *Journal of Geophysical Research: Space Physics, 114*(A03212). https://doi.org/10.1029/2008JA013776

Satori, G. (1996). Monitoring Schumann resonances-II. Daily and seasonal frequency variations. *Journal of Atmospheric and Terrestrial Physics, 58*(3), 1483-1488. https://doi.org/10.1016/0021-9169(95)00146-8

Schumann, W.O. (1952). On the free oscillations of a conducting sphere which is surrounded by an air layer and an ionosphere shell (in German). *Z. Naturforsch. B, 7A*, 149-154

Sentman, D.D. (1987). Magnetic elliptical polarization of Schumann resonances. *Radio Science, 22*(4), 595-606. https://doi.org/10.1029/RS022i004p00595

Shapiro, N.M. & Campillo, M. (2004). Emergence of broadband Rayleigh waves from correlations of the ambient seismic noise. *Geophysical Research Letters, 31*(L07614), 1-4. https://doi.org/10.1029/2004GL019491

Shiokawa, K., Otsuka, Y., Ogawa, T., & Wilkinson, P. (2004). Time evolution of high-altitude plasma bubbles imaged at geomagnetic conjugate points. *Annales Geophysicae, 29*(9), 3137-3143. https://doi.org/10.5194/angeo-22-3137-2004

Simoes, F., Pfaff, R. & Freudenreich, H. (2011). Satellite observations of Schumann resonances in the Earth's ionosphere. *Geophysical Research Letters, 38*(L22101) 1-5. https://doi.org/10.1029/2011GL049668

Surkov, V.V., Nosikova, N.S., Plyasov, A.A., Pilipenko, V.A. & Ignatov, V.N. (2013). Penetration of Schumann resonances into the upper atmosphere. *Journal of Atmospheric and Solar-Terrestrial Physics, 97*(May), 65-74. https://doi.org/10.1016/j.jastp.2013.02.015

Toffner-Clausen, L., Lesur, V., Olsen, N. & Finlay, C.C. (2016). In-flight scalar calibration and characterisation of the Swarm magnetometry package. *Earth, Planets and Space 68*(129). https://doi.org/10.1186/s40623-016-0501-6

Tsunoda, R.T. (1983). On the generation and growth of equatorial backscatter plumes: 2. Structuring of the west walls of upwellings. *Geophysical Research Letters, 88*(A6), 4869-4874. https://doi.org/10.1029/JA088iA06p04869

University of Iowa. (2022). *Waveform Calibrations*. Retrieved from EMFISIS An instrument suite on the Van Allen Probes: https://emfisis.physics.uiowa.edu/Waveform_Calibration

Wang, J., Huang, Q., Ma, Q., Chang, S., He, J., Wang, H., et al. (2020) Classification of VLF/LF Lightning Signals Using Sensors and Deep Learning Methods. *Sensors, 20*(4), 1030. https://doi.org/10.3390/s20041030

Woodman, R.F. (2009). Spread F - an old equatorial aeronomy problem finally resolved? *Ann. Geophysics 27*(5), 1915-1934. https://doi.org/10.5194/angeo-27-1915-2009

Woodman, R.F. and Hoz, C.L. Radar Observations of F Region Equatorial Irregularities. *Journal of Geophysical Research, 81*(31), 5447-5466. https://doi.org/10.1029/JA081i031p05447

Yokoyama, T., Yamamoto, M., Otsuka, Y., Nishioka, M., Tsugawa, T., Watanabe, S., & Pfaff, R.F. (2011). On postmidnight low-latitude ionospheric irregularities during solar minimum: 1. Equatorial Atmosphere Radar and GPS-TEC observations in Indonesia. *Journal of Geophysical Research, 116*, A11325. https://doi.org/10.1029/2011JA016797

Zheng, H., Holzworth, R.H., Brundell, J.B., Jacobson, A.R., Wygant, J.R., Hospodarsky, G.B. et al. (2015). A statistical study of whistler waves observed by Van Allen Probes (RBSP) and lightning detected by WWLN. *Journal of Geophysical Research: Space Physics, 121*(3), 2067-2079. https://doi.org/10.1002/2015JA022010

Figure 1. Dispersion relations computed from the De Jonghe and Keppens (2021a) two-fluid model are shown. The plasma parameters in the figure title are typical ionospheric conditions that correspond approximately to the conditions for the data shown in Figure **5**. The angle between the magnetic field and wavevector direction is θ. The three MHD wave modes are shown in green for ***S*** slow MS, red for ***A*** Alfven and blue for ***F*** fast MS waves; also shown in cyan for **O** ordinary, black for **X** extraordinary electromagnetic and magenta for M modified electrostatic waves. In **a**, **d** and **g**, the wave frequency is shown as a function of the wavenumber for the ion species listed in the legends. The cyclotron frequencies for each ion species are indicated next to the Ω_x labels. In **b**, **e** and **h** the frequency vs. phase velocity V_p is plotted with low frequency limit values for the slow, Alfven and fast velocities (V_s, V_a and V_f) indicated on each plot. In **c**, **f** and **i**, the frequency vs. inverse group velocity V_g is plotted. The dashed lines in **b**, **e**, **h** and **c**, **f**, **g** show that the dispersion constants indicated in the legends reasonably fit the whistling regions for all three ion species.

Figure 2. The wave normal surfaces for phase and group velocities in pure O^+ plasma are shown using the same plasma parameters as the previous figure. The coordinate plane is chosen to contain the phase and group velocity vectors (Vp and Vg) as well as the magnetic field vector with the x axis along the ambient magnetic field direction. In **a**, **d** and **g** are shown the wave normal surfaces for the ***F*** waves for three choices of wavenumber. In **b**, **e**, and **h** the wave normal surfaces for ***A*** waves are shown while in **c**, **f**, and **i** the ***S*** wave normal surfaces are shown. In each of the subplots a characterization of the general behavior is given in the legend title.

Figure 3. The propagation of lightning generated (LG) waves through the atmosphere to their detection in the ionosphere is illustrated. The coordinates in this figure are altitude and latitude with longitude perpendicular to the plane of the page. The near field spherical wavefronts, from a representative strike at ground level and -24°N latitude, are indicated by the black semi-ovals (the coarse latitude scale distorts the circles). The trajectory of the Van Allen probe for the specific perigee pass involved in later figures **5**,**6**,**7**, and **8** is shown by the magenta line with circles drawn at the location of each data burst acquired during the perigee pass. The circle radii are proportional to the dispersion constant determined from whistlers within each data burst. For bursts having unusual nearly dispersionless spikes, black asterisks are plotted instead of magenta circles. The neutral region between the Earth's surface and the bottom of the ionosphere forms the Earth ionosphere waveguide (EIWG), in which most of the power of LG electromagnetic waves propagate. Within the EIWG, at long range, LG waves propagate as Q-bursts described by (Nickolaenko et al., 2004) and illustrated in supplemental Figure **S1**. Inside the region sketched in the figure as a hypothetical plasma bubble, nearly dispersionless spikes appear in the VAP scalograms. At the EIWG upper boundary (EIWGUB), energy in the form of plasma ***F*** waves refracts nearly vertically, as dictated by the much slower propagation speed at the entrance to the ionosphere than in the EIWG, and as seen in Figure **4**. Three examples of such ***F*** waves are illustrated by the blue arrows. The first blue arrow shows ***F*** waves that are longitudinally behind the plasma bubble. The second blue arrow shows ***F*** waves that reach the VAP while the VAP is located inside a plasma bubble. The third blue arrow over the higher latitude portion of the VAP trajectory is in a region of normal dispersion. Normal dispersion of ***F*** waves is proportional to

the integral $\int \sqrt{n_e/B}$ along the path from EIWGUB to the VAP detectors. Low frequency plasma ***S*** waves and ***A*** waves constrained by the magnetic field follow paths such as indicated by the representative dashed red line emerging from the EIWGUB near -16.4°N. With increasing altitude, the ionospheric composition changes substantially as plotted quantitatively in Figure **4**. At the EIWGUB entrance to the ionosphere, NO^+ ions dominate the composition, so that the cyclotron frequency for NO^+ dictates the relevant cutoff frequencies shown in Figure **1i**. As the plasma parameters change with altitude, the wave propagation slow and fast speeds V_s and V_f change but the qualitative separation between nearly vertical fast speed ***F*** waves and field aligned low frequency ***S*** and ***A*** waves persists. The Swarm-Bravo (SwB) altitude at the time of mysterious chirping is indicated by the green dashed line.

Figure 4. The plasma conditions are shown as a function of altitude for the time and location specified in the figure title. In **a**, the ion species percentages, and the ion, electron, and neutral temperatures are shown. In **b** the magnetic field strength and plasma density are shown. In **c** the two-fluid estimates for the slow speed V_s are shown for the three dominant ion species. In **d** the two-fluid estimates for the fast speed V_f are shown. In **e** the plasma β parameter is plotted as a function of altitude. The rapid increase in β at the entry to the ionosphere, together with the (Akhtar et al., 2021) theory in which ***S*** waves grow, while ***F*** waves shrink as β increases, suggests a mechanism to produce the globally distributed population of ***S*** waves in the ionosphere claimed in the present work.

Figure 5. Scalograms for a representative consecutive pair of bursts are shown. In **a**, **b**, and **c** scalograms for the U, V, and W components of magnetic field data are shown. In **d**, **e**, and **f** the electric field scalograms are shown. In **g** the orientation of the probe spin vector is shown by the cyan $\sin(\delta)$ and magenta $\cos(\lambda)$ curves which become unity when the W / U axes respectively align with the local magnetic field as indicated in the **5g** legend. Just over one full rotation of the VAP probe occurs over the 12 s period in this figure. The location of VAP-A at the start of this period is indicated in geodetic coordinates. Horizontal white dashed lines in the scalogram plots are drawn at the cyclotron frequencies Ω_H and Ω_O. The curved dashed white lines drawn over the scalograms have $\Delta T = DC/\sqrt{f}$ with various dispersion constants (*DC*). The minimum *DC* value is indicated in the upper left-hand corner of each scalogram. The two early low dispersion (DC=0.1) whistlers seen near 9:16:01 are marked with white vertical dashed lines extending only up to Ω_O in order not to obscure their signals at higher frequency. At frequencies below the cone of influence (COI) indicated by the curved black dashed lines superimposed on each scalogram plot, the amplitudes are derived under the assumption that the time variations in the burst data are symmetric about the boundaries at the start and end of the burst data. Below the COI, scalogram amplitudes must be viewed with caution. The nearly vanishing amplitudes seen in all components at the middle of the scalogram plots is an artifact of the linear interpolation across the dead time gap between successive bursts.

Figure 6. Spectrograms of the electromagnetic field from EMFISIS data are shown from a series of 100 successive bursts of Van Allen Probe-A (VAP-A) data. In **a**, **b**, and **c**, spectrograms for the three components (U, V and W) of the magnetic field are displayed. In **d**, **e** and **f**, electric field spectrograms are displayed. In **g** are plotted the *DC*s (dispersion constants) determined to fit

individual whistlers clearly correlated with specific lightning strokes occurring within each burst period. In a few cases after 9:19, no clearly correlated whistler/lightning stroke pair is found, and a *DC* value is not plotted. The model *DC* values are computed using IRI (with IGRF-13 coefficients) magnetic field and plasma densities along vertical paths to the indicated altitude. In **h** the altitude and longitude of VAP-A for each burst are plotted as a function of time with the latitudes for the first and last bursts indicated in the legend title. The specific bursts shown as scalograms in Figures **5** and **8** are indicated by blue arrows.

Figure 7. Representative fully calibrated spectra are displayed for four samples of data from the perigee pass spectrograms shown in the previous figure. Magnetic field spectra are shown in **a**, **d**, **g** and **j** with the time interval involved in each spectrum listed in the legend title for each case. Electric field spectra from the same four periods are shown in **b**, **e**, **h** and **k**. The RPA estimated upper limit on phase velocity as a function of frequency is shown in **c**, **f**, **i** and **l**.

Figure 8. Scalograms with the same layout as Figure **5** for the burst represented by the spectra in the fourth column of Figure **7**. For most of this burst, many dispersionless spikes are seen, but only a single significant whistler near the end of the burst is significant. None of the 49 WWLLN detected lighting strokes (at times indicated by the white dashed curves using the *DC* value indicated in the figure title) are seen as whistlers in this plot. One low dispersion whistler not detected by the WWLLN is seen near the end of this time interval.

Figure 9. Scalograms with the same layout as Figure **5** for the burst corresponding to a passage through a particularly strong flash. This flash comprised 10 strokes detected by the WWLLN and 19 groups detected by the GLM. The timing and intensities of these strokes and groups are shown in supplemental Figure **S4**.

Figure 10. Scalograms for the two WERA magnetic field components, along with their time resolved values are shown for the 0.57 s interval containing all the GLM groups associated with the single flash described in the previous figure. In **a** and **c** scalograms for the North/South (NS) & East/West (EW) components of magnetic field are shown. Dispersion curves using the *DC* value in the figure title are superposed for each of the 10 WWLLN detected strokes during this interval. In **b** and **d** the NS and EW magnetic fields are plotted as a function of time. In **f** the summation of the azimuthal magnetic field contributions from the 10 WWLLN detected strokes during this time using the (Nickolaenko et al. 2004) model is plotted. In **e** the scalogram of the temporal function plotted in **f** is shown.

Figure 11. Scalograms for the three electric field components, along with their time resolved values are shown for a 0.3 s interval for which three strong WWLLN detections are found while VAP lies within the hypothetical plasma bubble. In **a**, **c**, and **e** scalograms for the U, V, and W components of electric field data are shown. Superposed over the scalogram plots are the

dispersion curves for whistlers using the *DC* value in the figure title together with propagation delay from the WWLLN detected location to the VAP sub-satellite point. In **b**, **d**, and **f** the U, V, and W components of electric field data are shown as a function of time. In **g** the summation of the radial electric field contributions from the three WWLLN detected lightning strokes using the (Nickolaenko et al., 2004) theory for Q-bursts is plotted as a function of time.

Figure 12. The long-term variations in electric and magnetic ionospheric PSDs derived from the survey data are shown. For the 1st and 14th of each month throughout the VAP mission, the mean PSD over altitudes less than 1 Mm is computed form the survey mode data and displayed as a function of frequency. In **a**, **b**, and **c** the B_u, B_v and B_w PSDs are shown. In **d**, **e**, and **f** the E_u, E_v, and E_w PSDs are shown. In **g** the latitude and local solar time of perigee are shown. In **h** the altitude of perigee is shown.

Figure 13. The correlation in rms magnetic field fluctuations with location is shown. The correlation with altitude is shown in **a**, with longitude in **b**, and with magnetic latitude in **c**.

Figure 14. Spectrograms of data from the VFM magnetometers of the SwB satellite are shown for a six-hour period around the onset of chirping. In **a**, **b** and **c**, the VFM-x, -y and -z channel spectrograms are shown. In **d** the cosine of the angle between the local magnetic field and the satellite velocity vector is plotted in red with the ordinate scale on the right-hand side. Also plotted in black with ordinate on the left-hand side is a model of the doppler shifted fundamental Schumann resonance frequency. In **e** the magnitude of the VFM-y channel is plotted as a function of time. In **f** the latitude and longitude of SwB and the magnitude of the local magnetic field is plotted as a function of time. At each ascending or descending node (marked with asterisks) the local solar time and longitude are called out.

Figure 1.

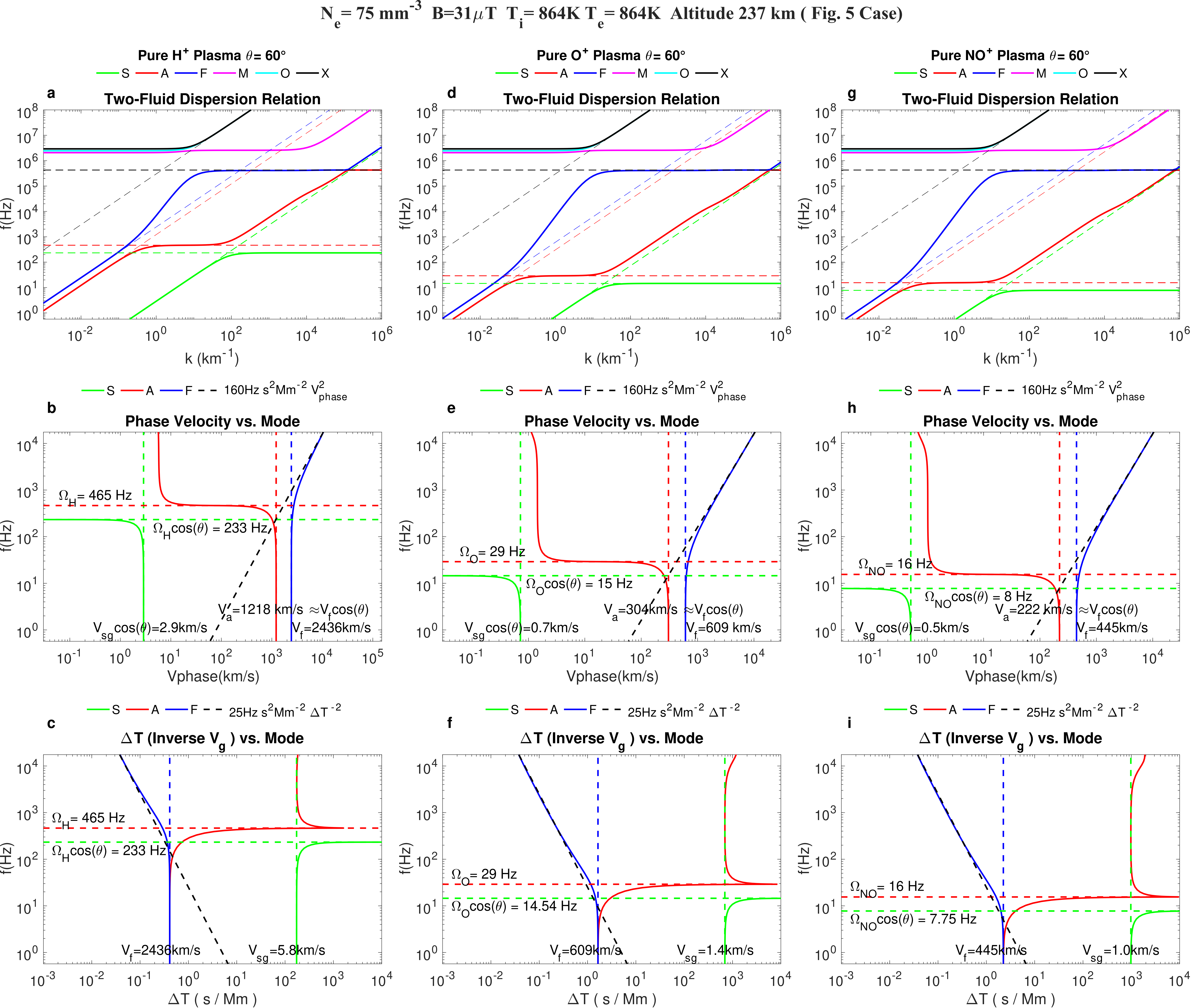

N_e = 75 mm^-3 B=31μT T_i = 864K T_e = 864K Altitude 237 km (Fig. 5 Case)
Pure H+ Plasma θ= 60°
Pure O+ Plasma θ= 60°
Pure NO+ Plasma θ= 60°
S A F M O X
a
d
g
Two-Fluid Dispersion Relation
f(Hz)
k (km^-1)
S A F 160Hz s^2Mm^-2 V^2_phase
b
e
h
Phase Velocity vs. Mode
Ω_H= 465 Hz
Ω_H cos(θ) = 233 Hz
V_a=1218 km/s ≈V_f cos(θ)
V_sg cos(θ)=2.9km/s
V_f=2436km/s
Ω_O= 29 Hz
Ω_O cos(θ) = 15 Hz
V_a=304km/s ≈V_f cos(θ)
V_sg cos(θ)=0.7km/s
V_f=609 km/s
Ω_NO= 16 Hz
Ω_NO cos(θ) = 8 Hz
V_a=222 km/s ≈V_f cos(θ)
V_sg cos(θ)=0.5km/s
V_f=445km/s
Vphase(km/s)
S A F 25Hz s^2Mm^-2 ΔT^-2
c
f
i
ΔT (Inverse V_g) vs. Mode
Ω_H= 465 Hz
Ω_H cos(θ) = 233 Hz
V_f=2436km/s
V_sg=5.8km/s
Ω_O= 29 Hz
Ω_O cos(θ) = 14.54 Hz
V_f=609km/s
V_sg=1.4km/s
Ω_NO= 16 Hz
Ω_NO cos(θ) = 7.75 Hz
V_f=445km/s
V_sg=1.0km/s
ΔT (s / Mm)

Figure 2.

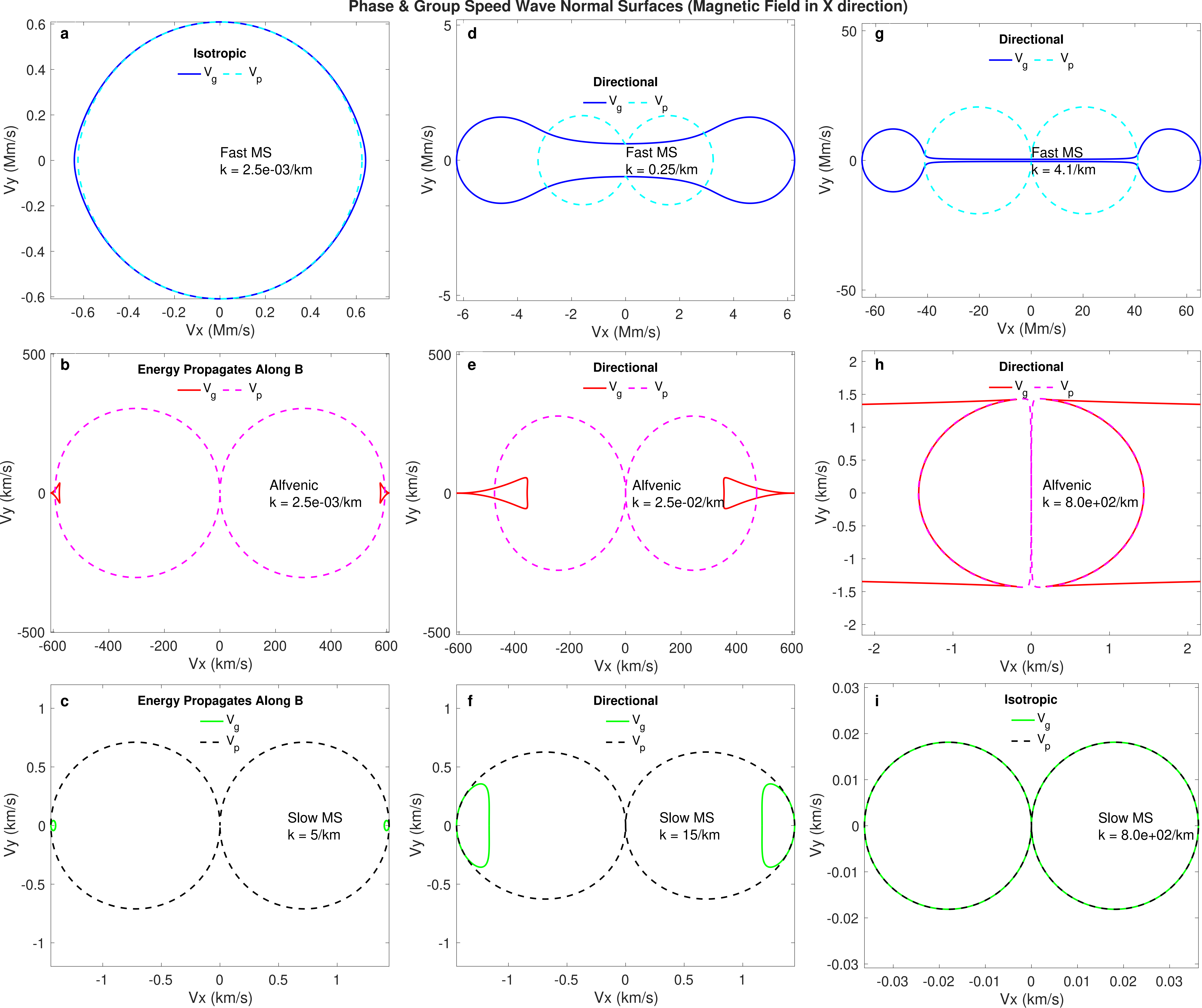
Phase & Group Speed Wave Normal Surfaces (Magnetic Field in X direction)
a
Isotropic
Vg Vp
Fast MS
k = 2.5e-03/km
Vy (Mm/s)
Vx (Mm/s)
d
Directional
Vg Vp
Fast MS
k = 0.25/km
Vy (Mm/s)
Vx (Mm/s)
g
Directional
Vg Vp
Fast MS
k = 4.1/km
Vy (Mm/s)
Vx (Mm/s)
b
Energy Propagates Along B
Vg Vp
Alfvenic
k = 2.5e-03/km
Vy (km/s)
Vx (km/s)
e
Directional
Vg Vp
Alfvenic
k = 2.5e-02/km
Vy (km/s)
Vx (km/s)
h
Directional
Vg Vp
Alfvenic
k = 8.0e+02/km
Vy (km/s)
Vx (km/s)
c
Energy Propagates Along B
Vg
Vp
Slow MS
k = 5/km
Vy (km/s)
Vx (km/s)
f
Directional
Vg
Vp
Slow MS
k = 15/km
Vy (km/s)
Vx (km/s)
i
Isotropic
Vg
Vp
Slow MS
k = 8.0e+02/km
Vy (km/s)
Vx (km/s)

Figure 3.

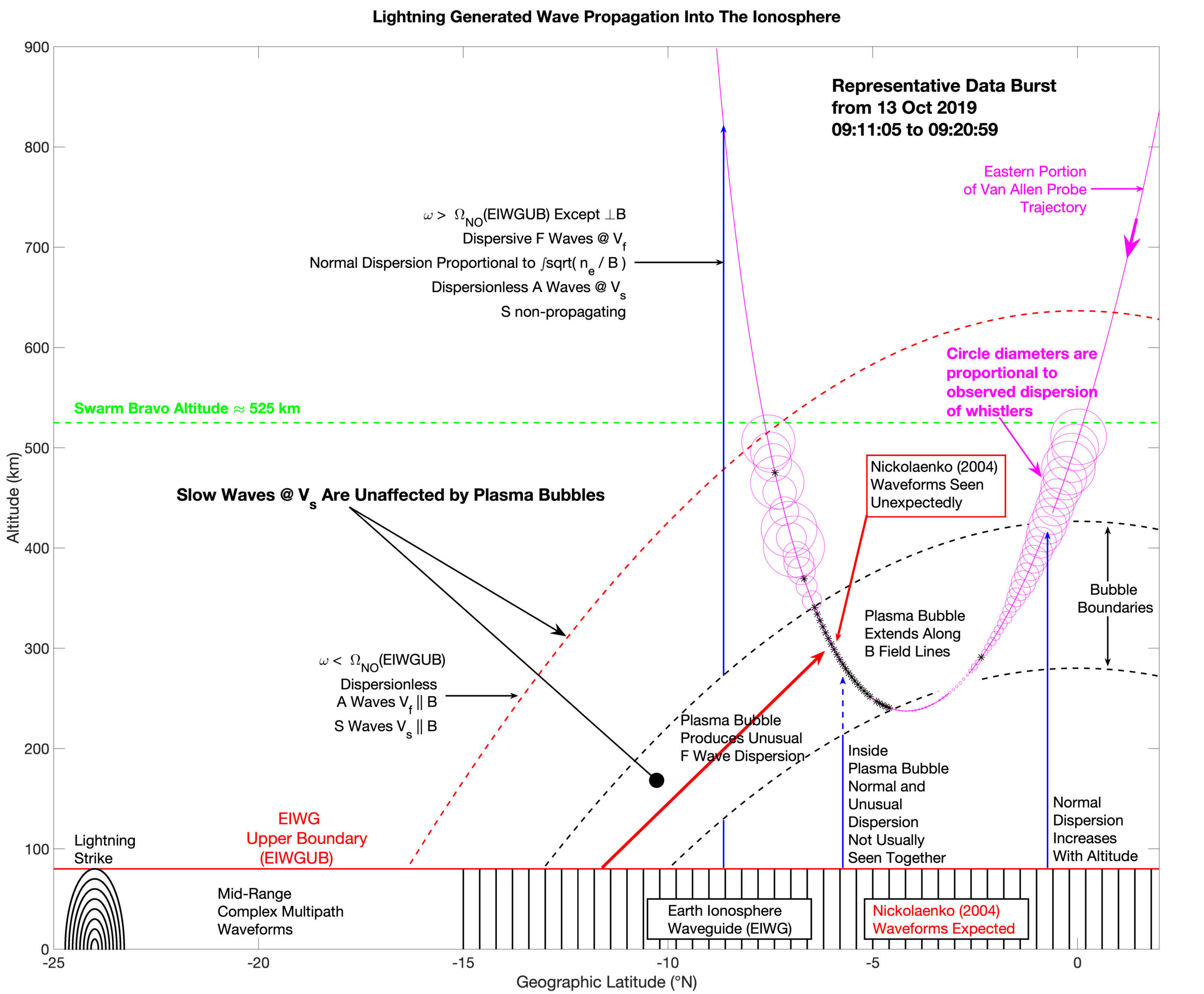

Lightning Generated Wave Propagation Into The Ionosphere
Representative Data Burst from 13 Oct 2019 09:11:05 to 09:20:59
Eastern Portion of Van Allen Probe Trajectory
$\omega > \Omega_{NO}$(EIWGUB) Except $\perp$B
Dispersive F Waves @ V_f
Normal Dispersion Proportional to $\int$sqrt(n_e / B)
Dispersionless A Waves @ V_s
S non-propagating
Circle diameters are proportional to observed dispersion of whistlers
Swarm Bravo Altitude ≈ 525 km
Slow Waves @ V_s Are Unaffected by Plasma Bubbles
Nickolaenko (2004) Waveforms Seen Unexpectedly
Plasma Bubble Extends Along B Field Lines
Bubble Boundaries
$\omega < \Omega_{NO}$(EIWGUB)
Dispersionless
A Waves V_f || B
S Waves V_s || B
Plasma Bubble Produces Unusual F Wave Dispersion
Inside Plasma Bubble Normal and Unusual Dispersion Not Usually Seen Together
Normal Dispersion Increases With Altitude
EIWG Upper Boundary (EIWGUB)
Lightning Strike
Mid-Range Complex Multipath Waveforms
Earth Ionosphere Waveguide (EIWG)
Nickolaenko (2004) Waveforms Expected
Altitude (km)
Geographic Latitude (°N)
0
100
200
300
400
500
600
700
800
900
-25
-20
-15
-10
-5
0

Figure 4.

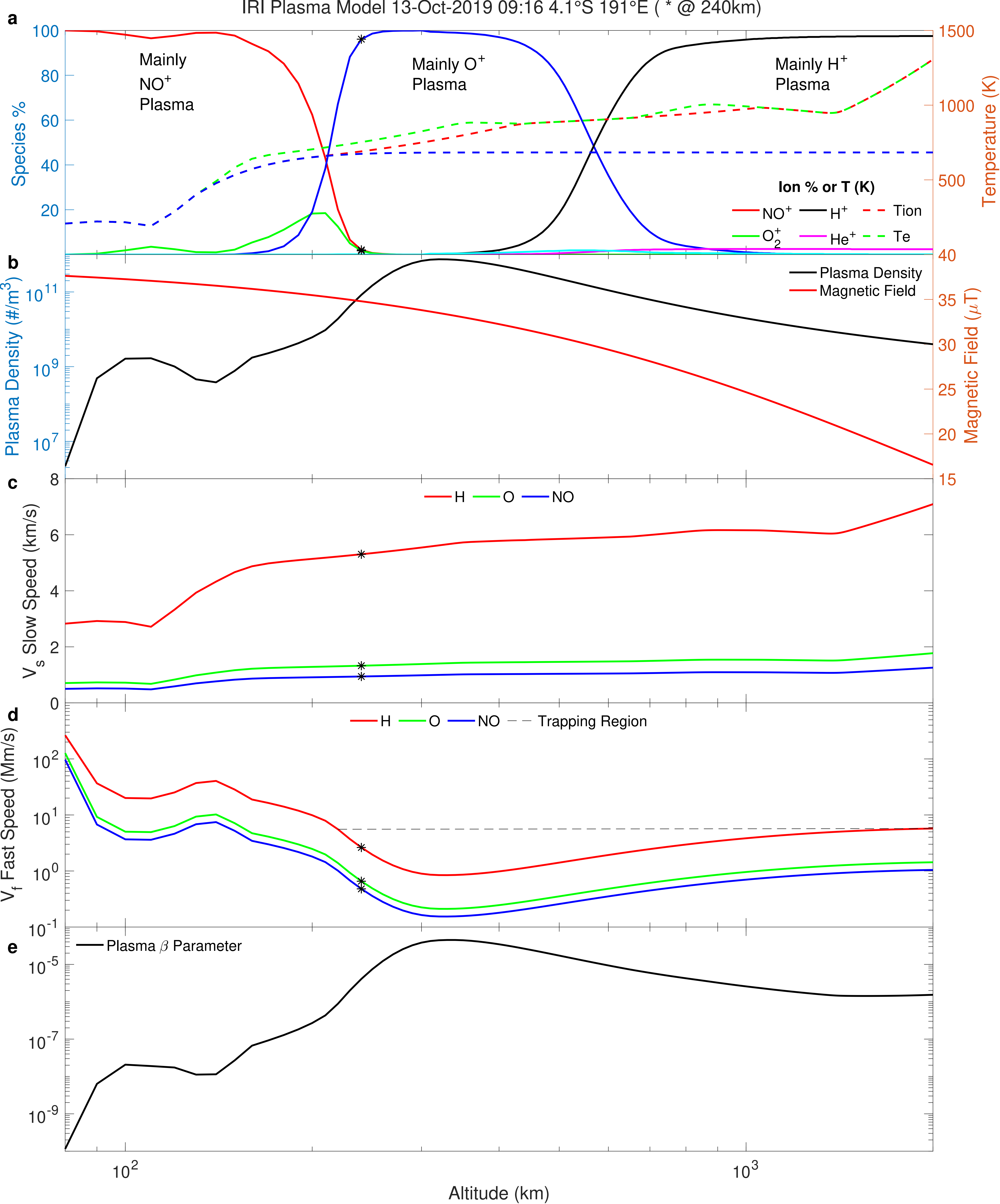
IRI Plasma Model 13-Oct-2019 09:16 4.1°S 191°E (* @ 240km)
a
Mainly NO+ Plasma
Mainly O+ Plasma
Mainly H+ Plasma
Species %
Temperature (K)
Ion % or T (K)
NO+
H+
Tion
O2+
He+
Te
b
Plasma Density
Magnetic Field
Plasma Density (#/m3)
Magnetic Field (μT)
c
H
O
NO
Vs Slow Speed (km/s)
d
Trapping Region
Vf Fast Speed (Mm/s)
e
Plasma β Parameter
Altitude (km)

Figure 5.

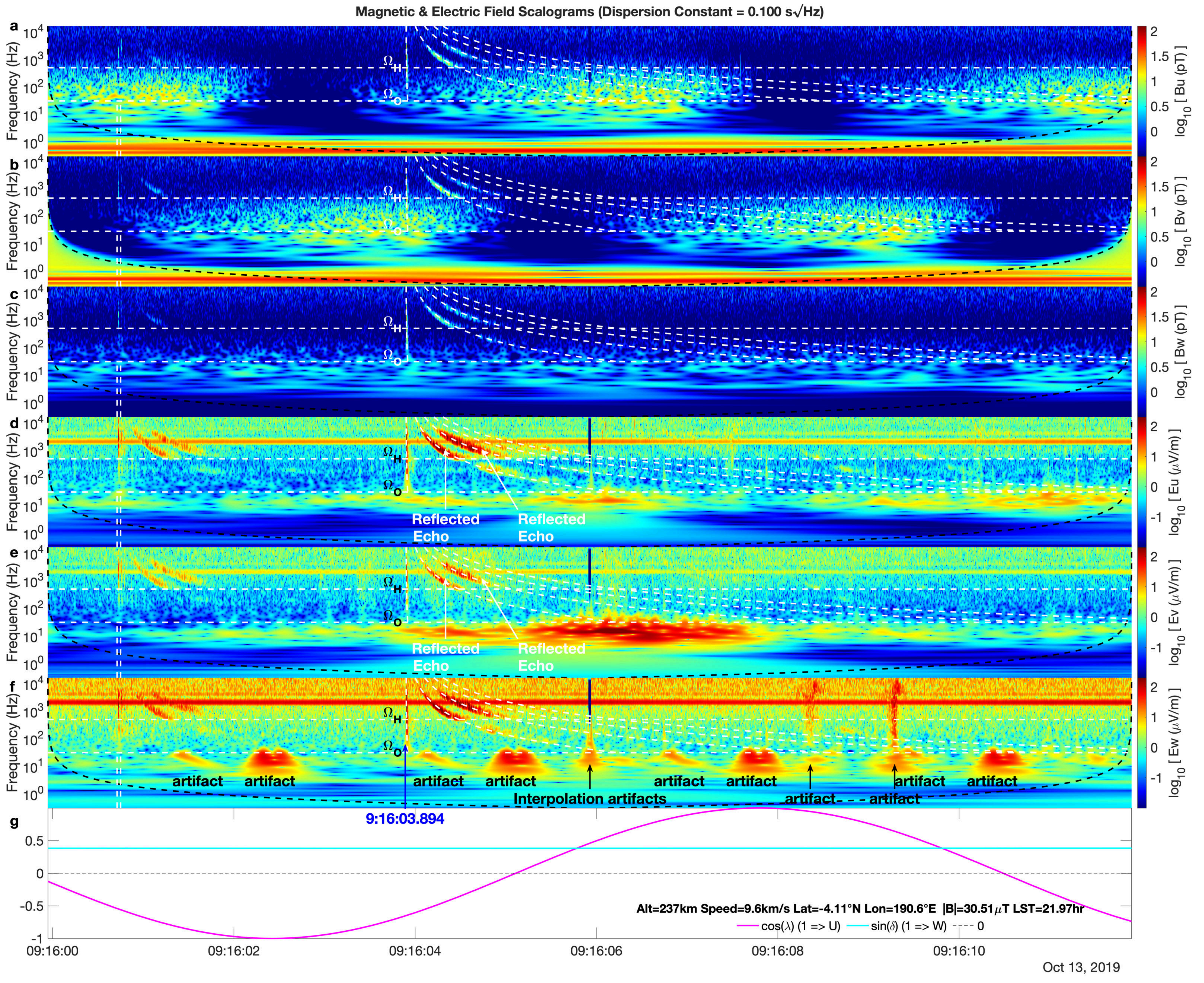

Magnetic & Electric Field Scalograms (Dispersion Constant = 0.100 s√Hz)
a
b
c
d
e
f
g
Frequency (Hz)
log10 [Bu (pT)]
log10 [Bv (pT)]
log10 [Bw (pT)]
log10 [Eu (μV/m)]
log10 [Ev (μV/m)]
log10 [Ew (μV/m)]
ΩH
ΩO
Reflected Echo
Reflected Echo
artifact
Interpolation artifacts
9:16:03.894
Alt=237km Speed=9.6km/s Lat=-4.11°N Lon=190.6°E |B|=30.51μT LST=21.97hr
cos(λ) (1 => U)
sin(δ) (1 => W)
0
09:16:00
09:16:02
09:16:04
09:16:06
09:16:08
09:16:10
Oct 13, 2019

Figure 6.

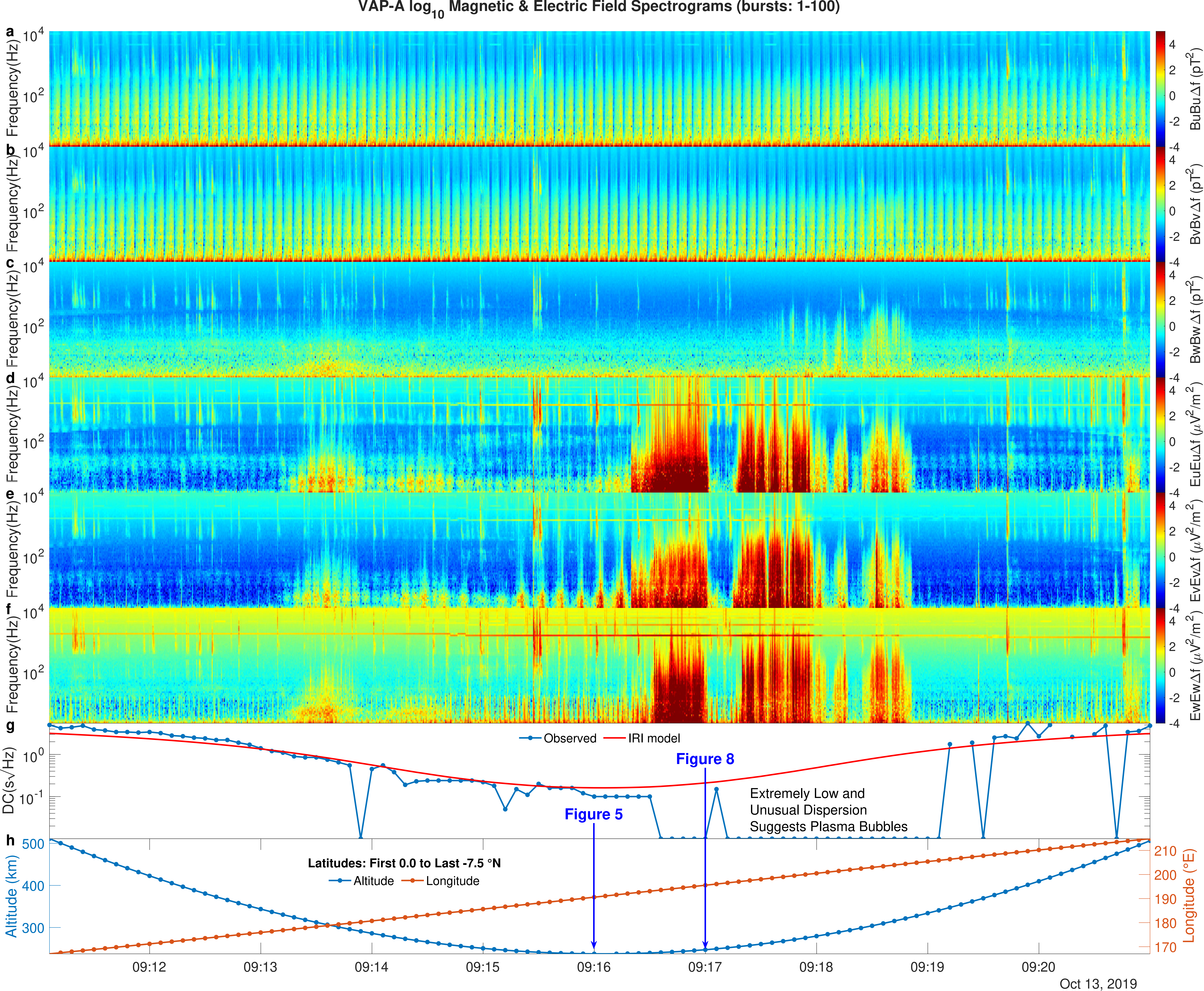

VAP-A $\log_{10}$ Magnetic & Electric Field Spectrograms (bursts: 1-100)
a
b
c
d
e
f
g
h
Frequency(Hz)
10^4
10^2
BuBu∆f (pT^2)
BvBv∆f (pT^2)
BwBw∆f (pT^2)
EuEu∆f ($\mu V^2/m^2$)
EvEv∆f ($\mu V^2/m^2$)
EwEw∆f ($\mu V^2/m^2$)
4
2
0
-2
-4
Observed
IRI model
DC(s√Hz)
10^0
10^{-1}
Figure 8
Figure 5
Extremely Low and
Unusual Dispersion
Suggests Plasma Bubbles
Latitudes: First 0.0 to Last -7.5 °N
Altitude
Longitude
Altitude (km)
500
400
300
Longitude (°E)
210
200
190
180
170
09:12
09:13
09:14
09:15
09:16
09:17
09:18
09:19
09:20
Oct 13, 2019

Figure 7.

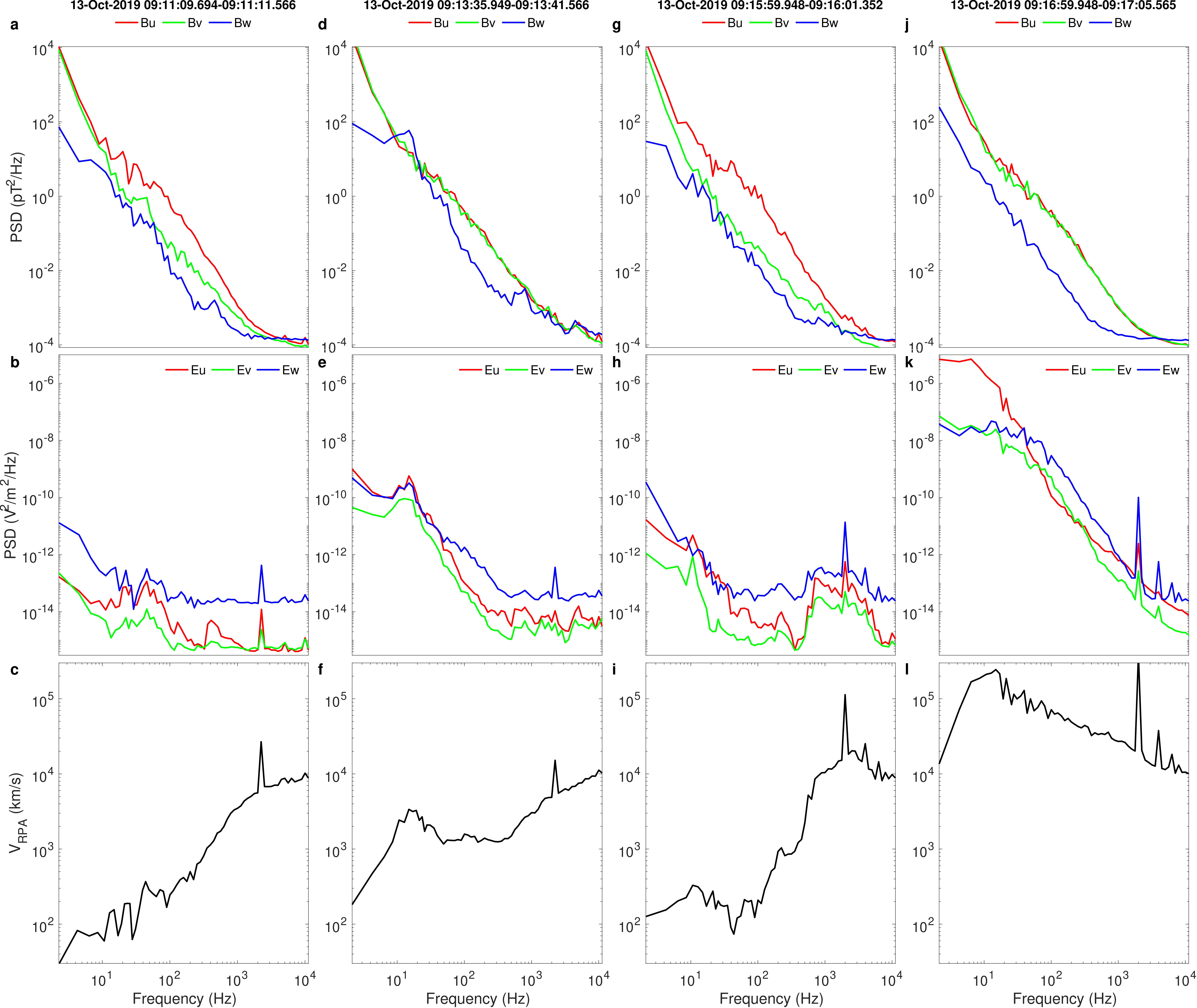
13-Oct-2019 09:11:09.694-09:11:11.566
13-Oct-2019 09:13:35.949-09:13:41.566
13-Oct-2019 09:15:59.948-09:16:01.352
13-Oct-2019 09:16:59.948-09:17:05.565
a
d
g
j
Bu Bv Bw
PSD (pT^2/Hz)
b
e
h
k
Eu Ev Ew
PSD (V^2/m^2/Hz)
c
f
i
l
V$_{RPA}$ (km/s)
Frequency (Hz)

Figure 8.

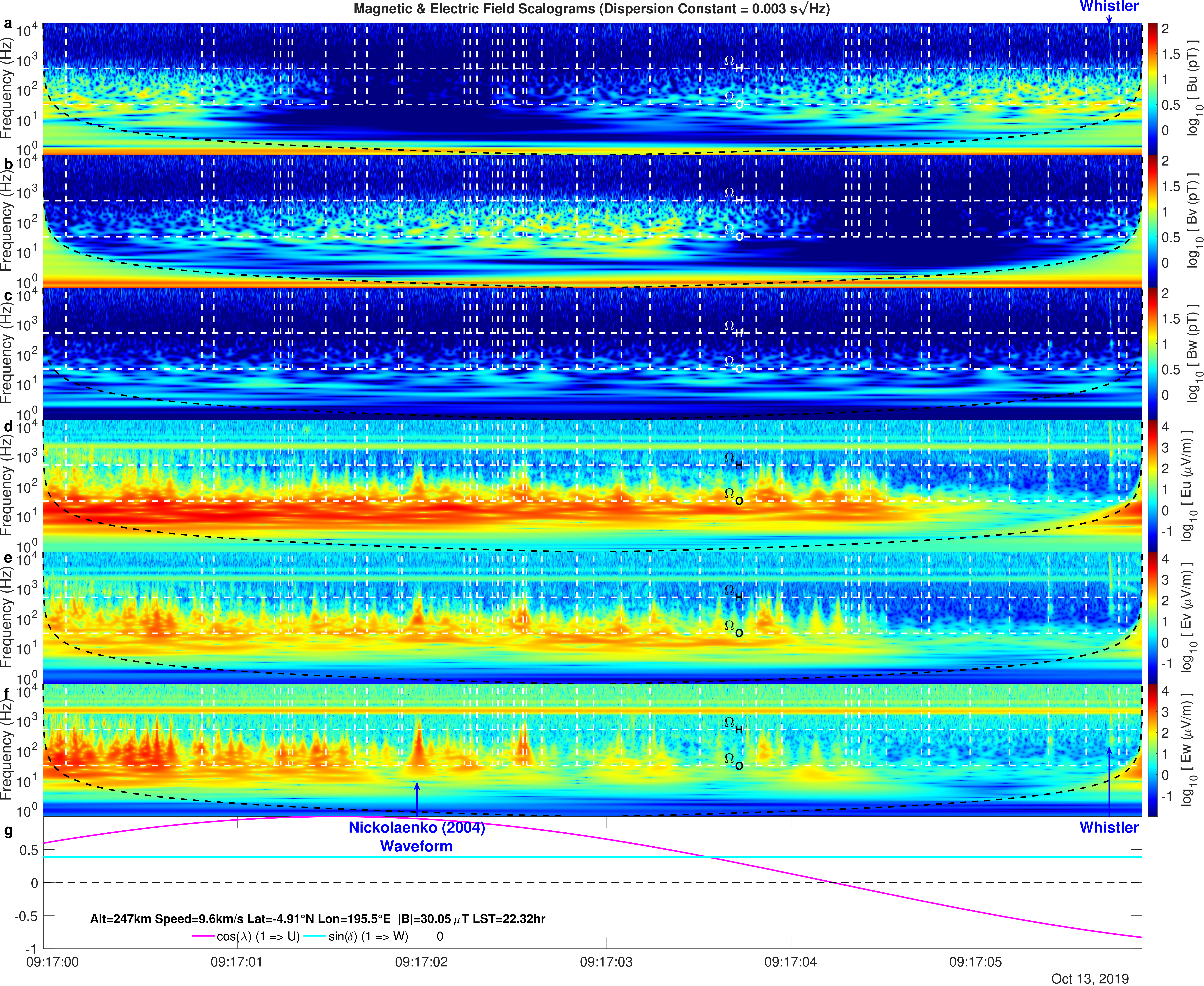

Magnetic & Electric Field Scalograms (Dispersion Constant = 0.003 s√Hz)
Whistler
a
b
c
d
e
f
g
Frequency (Hz)
log10 [Bu (pT)]
log10 [Bv (pT)]
log10 [Bw (pT)]
log10 [Eu (μV/m)]
log10 [Ev (μV/m)]
log10 [Ew (μV/m)]
Ω H
Ω O
Nickolaenko (2004)
Waveform
Whistler
Alt=247km Speed=9.6km/s Lat=-4.91°N Lon=195.5°E |B|=30.05 μT LST=22.32hr
cos(λ) (1 => U) sin(δ) (1 => W) 0
09:17:00
09:17:01
09:17:02
09:17:03
09:17:04
09:17:05
Oct 13, 2019

Figure 9.

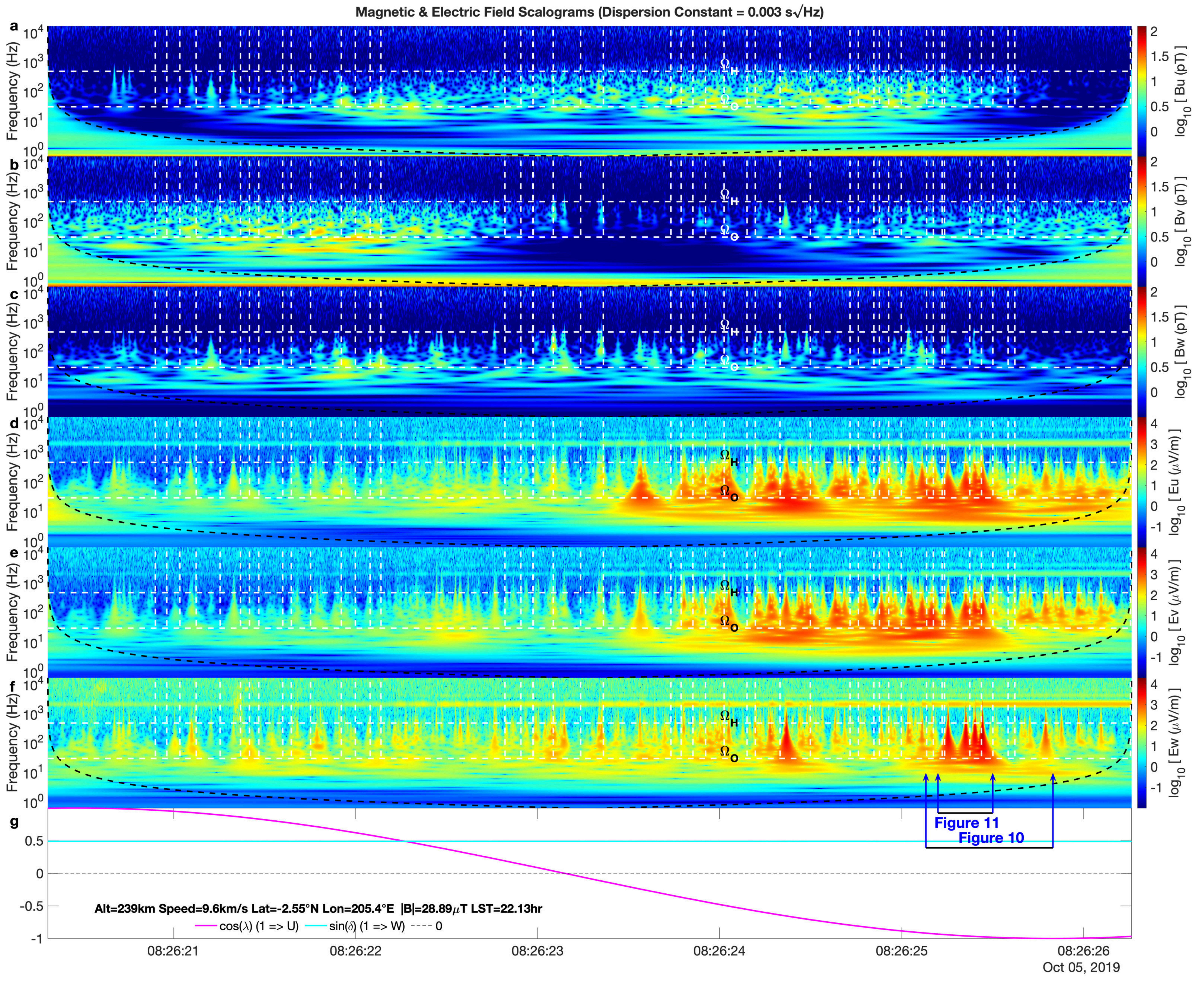
Magnetic & Electric Field Scalograms (Dispersion Constant = 0.003 s√Hz)
a
b
c
d
e
f
g
Frequency (Hz)
Ω_H
Ω_O
$\log_{10}$ [Bu (pT)]
$\log_{10}$ [Bv (pT)]
$\log_{10}$ [Bw (pT)]
$\log_{10}$ [Eu (μV/m)]
$\log_{10}$ [Ev (μV/m)]
$\log_{10}$ [Ew (μV/m)]
Figure 11
Figure 10
Alt=239km Speed=9.6km/s Lat=-2.55°N Lon=205.4°E |B|=28.89μT LST=22.13hr
cos(λ) (1 => U)
sin(δ) (1 => W)
0
08:26:21
08:26:22
08:26:23
08:26:24
08:26:25
08:26:26
Oct 05, 2019

Figure 10.

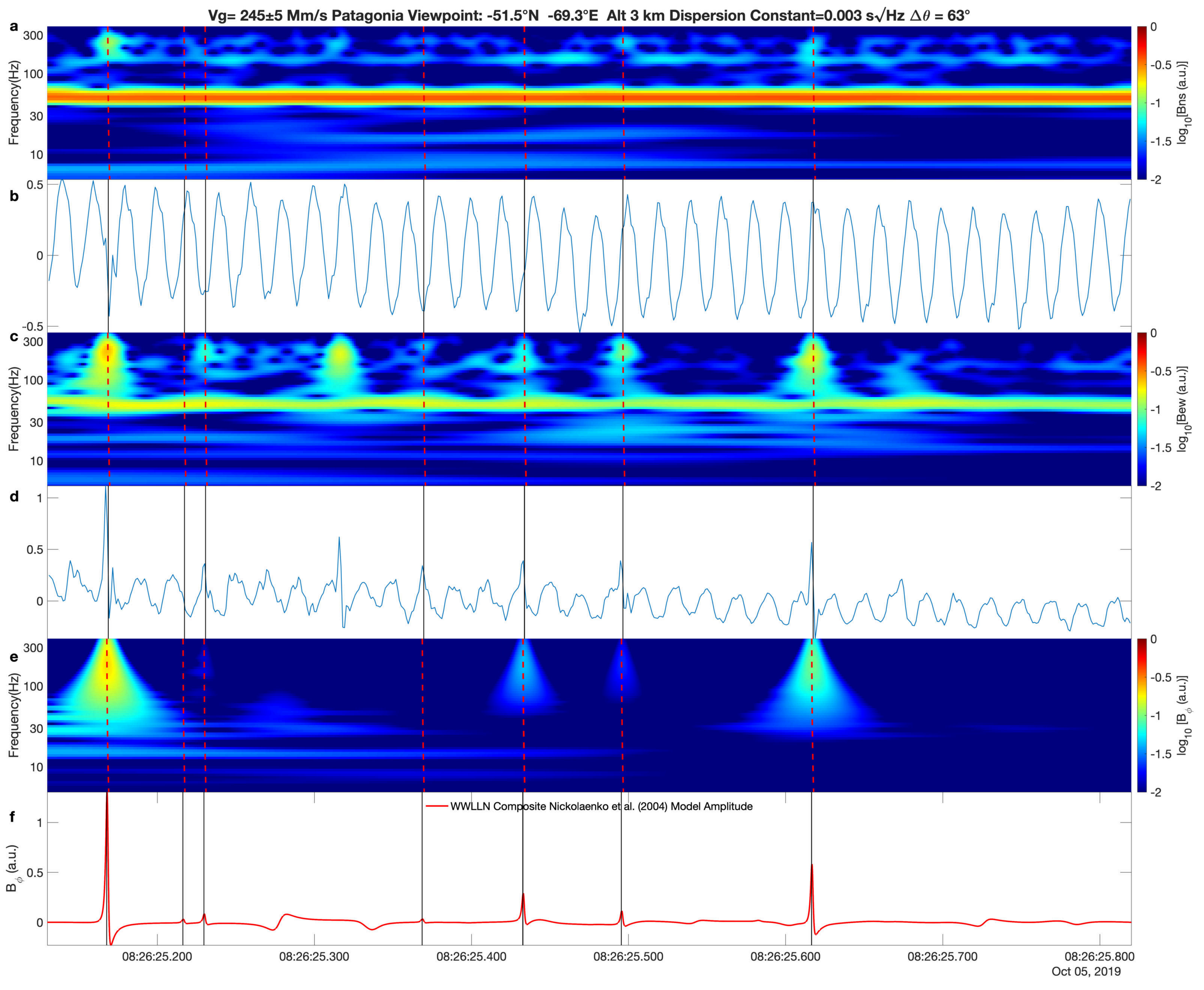
Vg= 245±5 Mm/s Patagonia Viewpoint: -51.5°N -69.3°E Alt 3 km Dispersion Constant=0.003 s√Hz Δθ = 63°
a
b
c
d
e
f
Frequency(Hz)
log10[Bns (a.u.)]
log10[Bew (a.u.)]
log10 [Bφ (a.u.)]
Bφ (a.u.)
WWLLN Composite Nickolaenko et al. (2004) Model Amplitude
08:26:25.200
08:26:25.300
08:26:25.400
08:26:25.500
08:26:25.600
08:26:25.700
08:26:25.800
Oct 05, 2019

Figure 11.

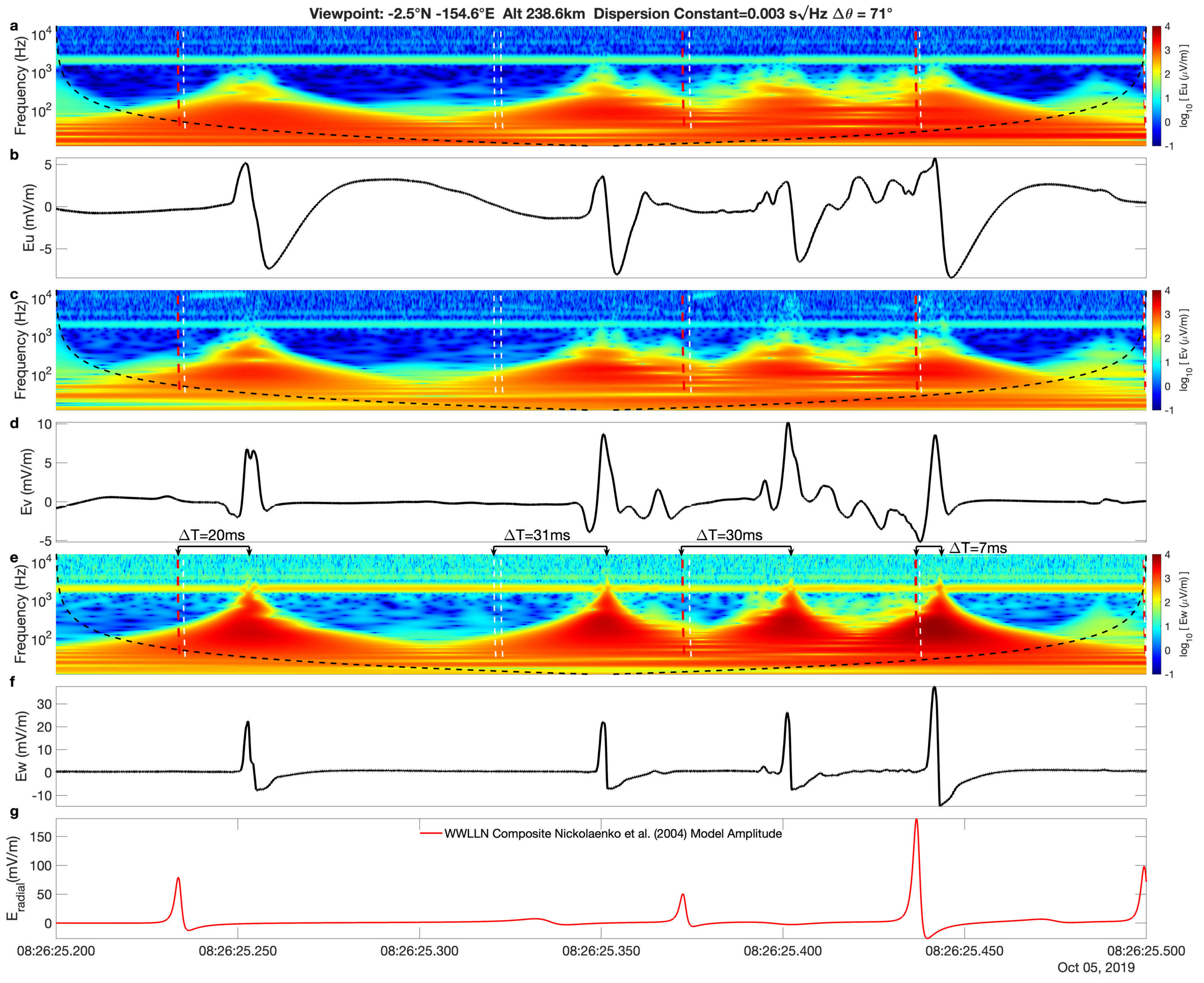

Viewpoint: -2.5°N -154.6°E Alt 238.6km Dispersion Constant=0.003 s√Hz Δθ = 71°
a
b
c
d
e
f
g
Frequency (Hz)
log10 [Eu (μV/m)]
Eu (mV/m)
log10 [Ev (μV/m)]
Ev (mV/m)
ΔT=20ms
ΔT=31ms
ΔT=30ms
ΔT=7ms
log10 [Ew (μV/m)]
Ew (mV/m)
E_radial (mV/m)
WWLLN Composite Nickolaenko et al. (2004) Model Amplitude
08:26:25.200
08:26:25.250
08:26:25.300
08:26:25.350
08:26:25.400
08:26:25.450
08:26:25.500
Oct 05, 2019

Figure 12.

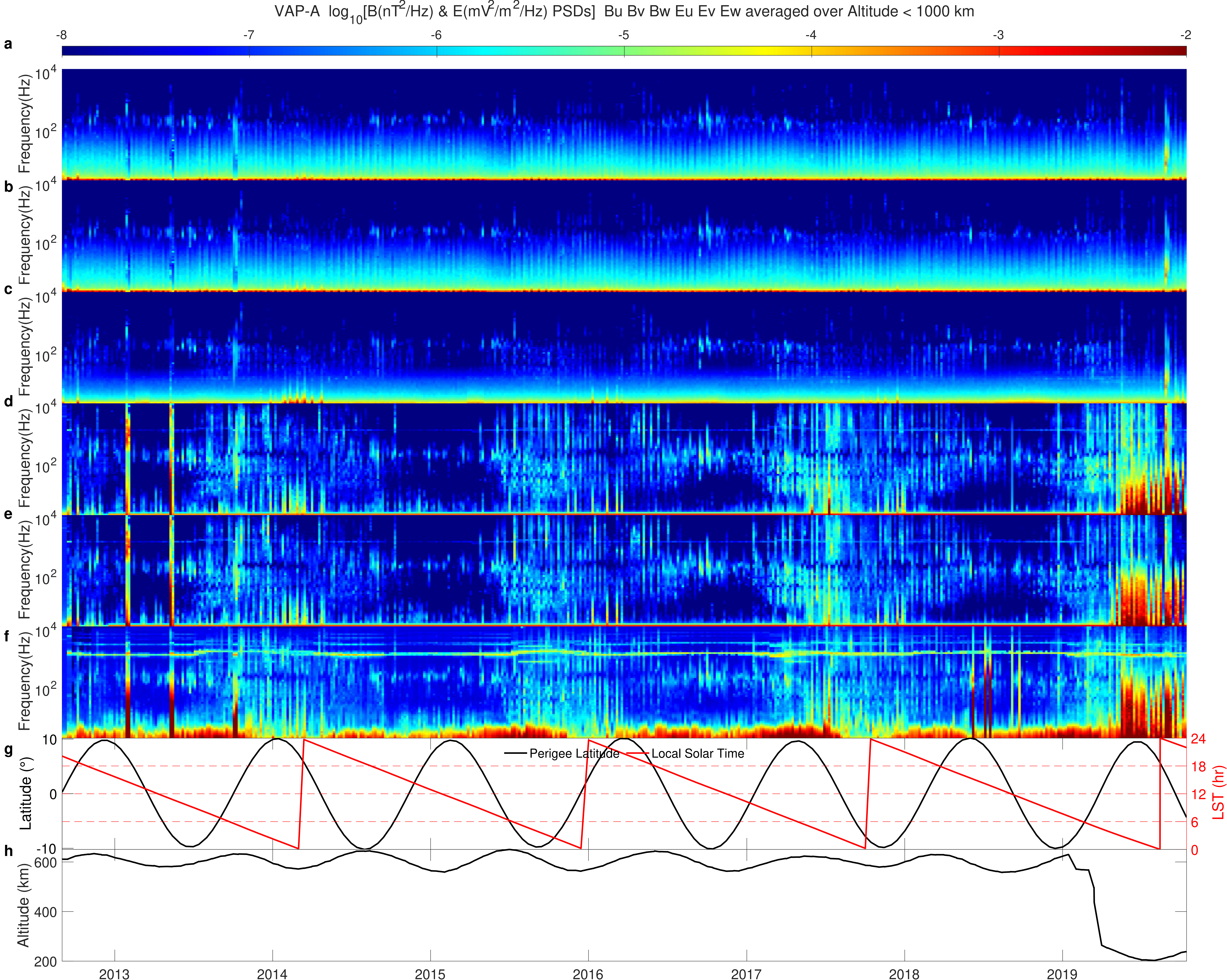

VAP-A log10[B(nT^2/Hz) & E(mV^2/m^2/Hz) PSDs] Bu Bv Bw Eu Ev Ew averaged over Altitude < 1000 km
-8
-7
-6
-5
-4
-3
-2
a
b
c
d
e
f
g
h
Frequency(Hz)
10^4
10^2
10
Perigee Latitude
Local Solar Time
Latitude (°)
LST (hr)
Altitude (km)
600
400
200
2013
2014
2015
2016
2017
2018
2019

Figure 13.

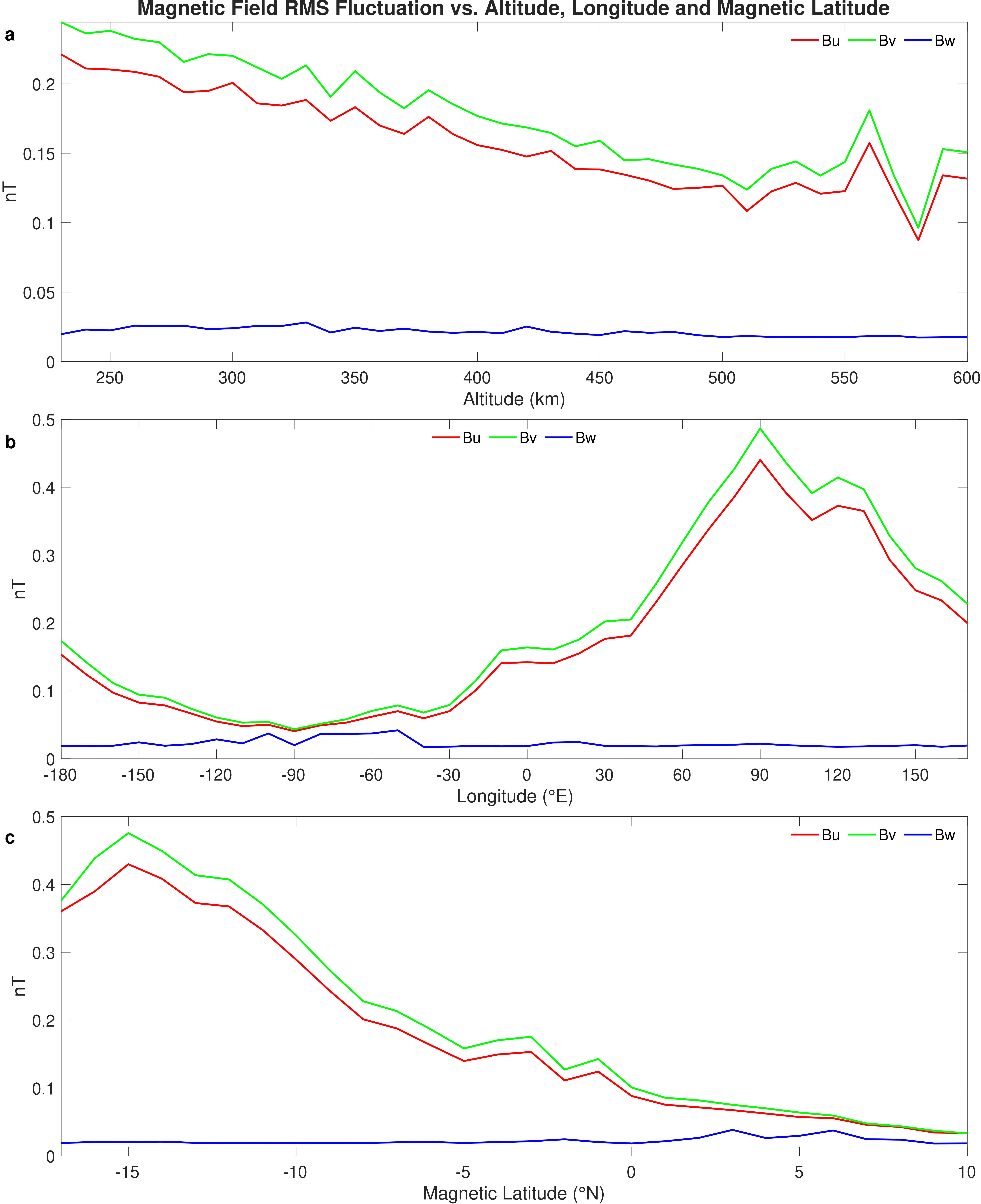

Magnetic Field RMS Fluctuation vs. Altitude, Longitude and Magnetic Latitude
a
Bu
Bv
Bw
nT
0
0.05
0.1
0.15
0.2
250
300
350
400
450
500
550
600
Altitude (km)
b
Bu
Bv
Bw
nT
0
0.1
0.2
0.3
0.4
0.5
-180
-150
-120
-90
-60
-30
0
30
60
90
120
150
Longitude (°E)
c
Bu
Bv
Bw
nT
0
0.1
0.2
0.3
0.4
0.5
-15
-10
-5
0
5
10
Magnetic Latitude (°N)

Figure 14.

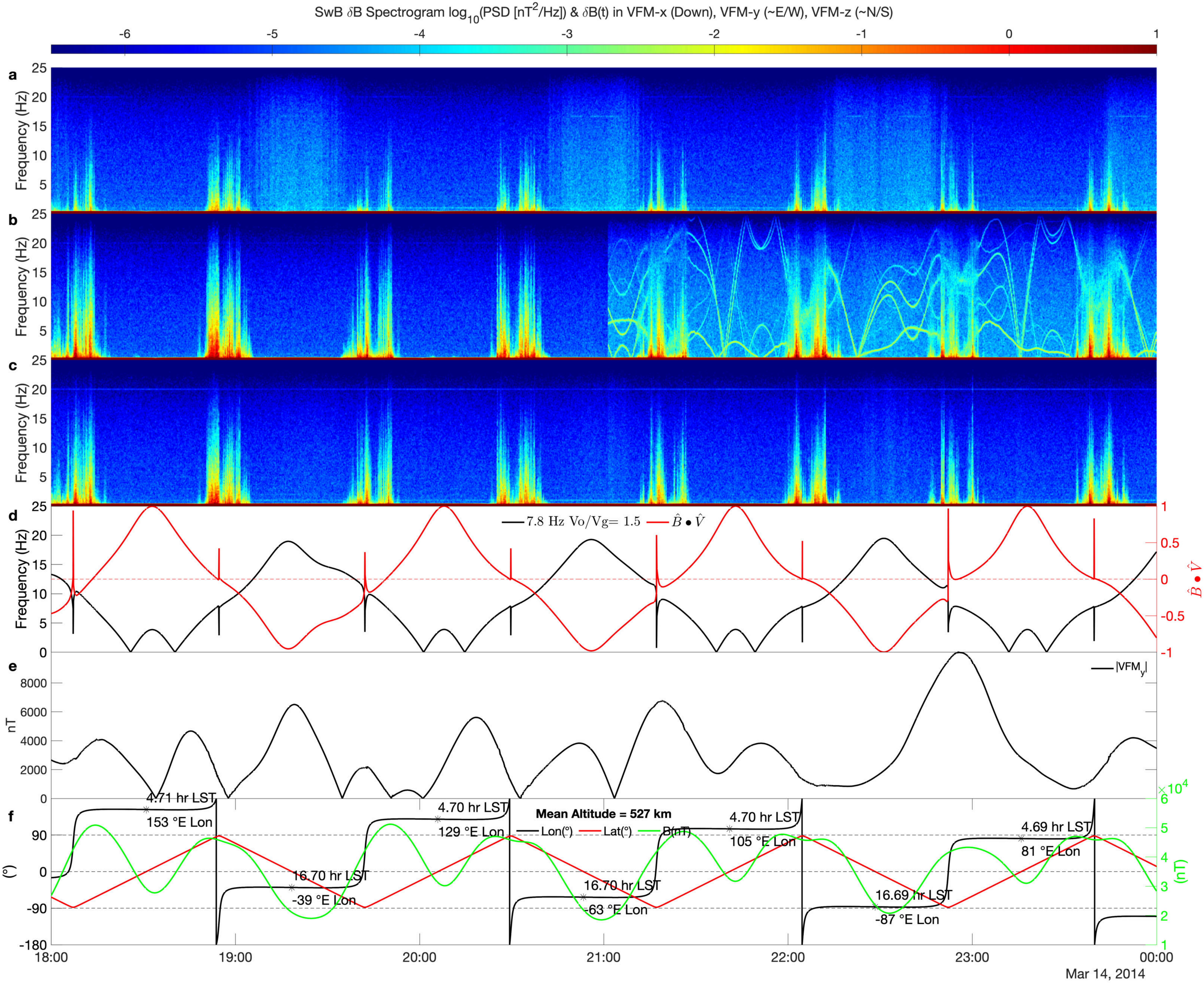

SwB δB Spectrogram log10(PSD [nT2/Hz]) & δB(t) in VFM-x (Down), VFM-y (~E/W), VFM-z (~N/S)
a
b
c
d
e
f
Frequency (Hz)
7.8 Hz Vo/Vg= 1.5
B̂ • V̂
|VFMy|
nT
Mean Altitude = 527 km
Lon(°)
Lat(°)
B(nT)
(°)
(nT)
×10^4
4.71 hr LST
153 °E Lon
4.70 hr LST
129 °E Lon
4.70 hr LST
105 °E Lon
4.69 hr LST
81 °E Lon
16.70 hr LST
-39 °E Lon
16.70 hr LST
-63 °E Lon
16.69 hr LST
-87 °E Lon
18:00
19:00
20:00
21:00
22:00
23:00
00:00
Mar 14, 2014

AGU PUBLICATIONS

Journal of Geophysical Research: Space Physics

Supporting Information for

A Novel Population of Slow Magnetosonic Waves and a Method for the Observation of the Roots of Plasma Bubbles in the Lower Ionosphere

Charles L. Bennett[1]

[1]Retired from Lawrence Livermore National Laboratory, Livermore CA

Contents of this file

Introduction

The text S1 in this supporting information provides a derivation of expression 7 in the main text.

The figures in this supporting information file supplement the main document.

Text S1.

Expression **6** from the main text is

$$DFR = \frac{\omega_o}{\omega} = 1 - \frac{V_o}{V_g}\frac{\hat{\boldsymbol{k}}\cdot\hat{\boldsymbol{V}}_o}{\hat{\boldsymbol{k}}\cdot\hat{\boldsymbol{B}}_{\boldsymbol{0}}}\,. \qquad (6)$$

This involves the ratio of the dot products of unit vectors $\hat{\boldsymbol{k}} \cdot \hat{\boldsymbol{V}}_o$ and $\hat{\boldsymbol{k}} \cdot \hat{\boldsymbol{B}}_\mathbf{0}$. The velocity and magnetic field vectors determine a plane. In the following, let the x axis be along the magnetic field direction and let the velocity vector be at an angle γ with respect to the magnetic field direction. The unit velocity vector in the x-y plane has coordinates

$$[\cos(\gamma), \sin(\gamma)],$$

so that for a unit wavevector $\hat{\boldsymbol{k}}$ in the x-y plane given by $[\cos(\theta), \sin(\theta)]$, the ratio of the dot products in expression (6) is

$$[\cos(\gamma)\cos(\theta)+ \sin(\gamma)\sin(\theta)]/\cos(\theta) = \cos(\gamma)+ \sin(\gamma)\tan(\theta).$$

Since components of the wavevector in the z direction orthogonal to the x-y plane make no difference to the DFR, without loss of generality, it can be assumed that the wavevector is confined to the x-y plane. The expression for the DFR in (**6**) has a central value that is independent of the wavevector direction θ given by

$$DFR=1- \cos(\gamma)\, V_o/V_g\ .$$

The spread of the DFR values about this central value is determined by $t=\tan(\theta)$. Although angles θ near $\pm\pi/2$ produce very large DFR values, the resulting DFR values are widely spread per unit change in θ. For a uniformly distributed random set of wave vector directions, the density of DFR values is given by the derivative of the arctangent function

$$\frac{d}{dt}\arctan(t) = \frac{1}{(1+t^2)}\ .$$

After supplying the offsets and scaling factors, this leads to the probability distribution in expression 7 of the main text

$$pdf \propto \frac{1}{\left(DFR-1+\frac{V_o}{V_g}\cos(\gamma)\right)^2+\left(\frac{V_o}{V_g}\sin(\gamma)\right)^2}\ . \tag{7}$$

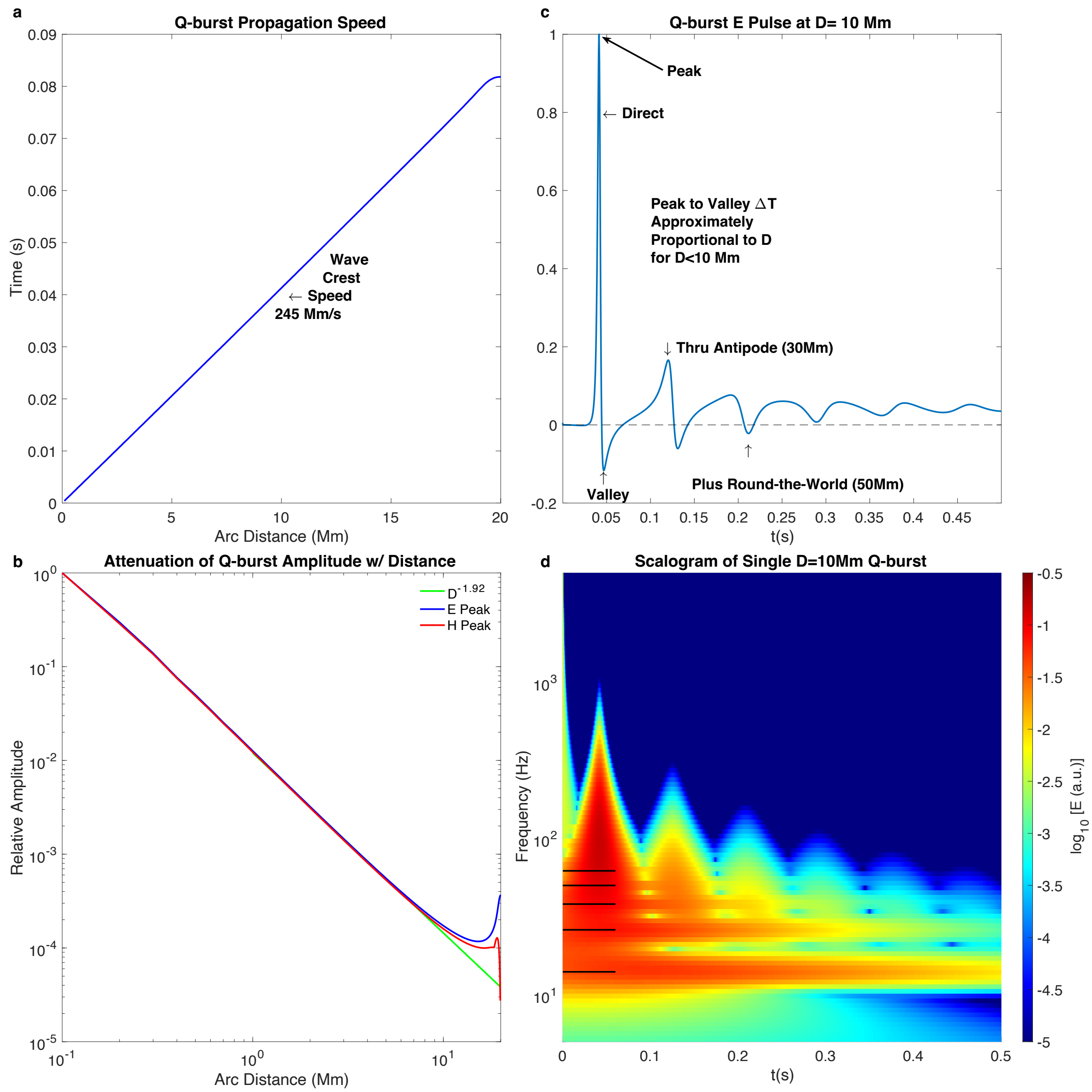

Figure S1. The evolution of a Q-burst is shown. In **a**, the time vs. distance of the peak of the earliest pulse is plotted. In **b**, the relative amplitudes for both electric and magnetic fields are plotted as a function of distance. In **c**, the electric field waveform at the equatorial arc-distance 10 Mm is plotted as a function of time. In **d**, a scalogram of the waveform shown in **c** is plotted. The scalogram intensity near t=0 is an artifact of the fast Fourier transform computation of the scalogram associated with the artificial jump in the electric field between the last and first times. The horizontal black lines superimposed on the scalogram show the even numbered Schumann Resonance frequencies, and illustrate that with full temporal resolution, even a single pulse contains Schumann Resonance information.

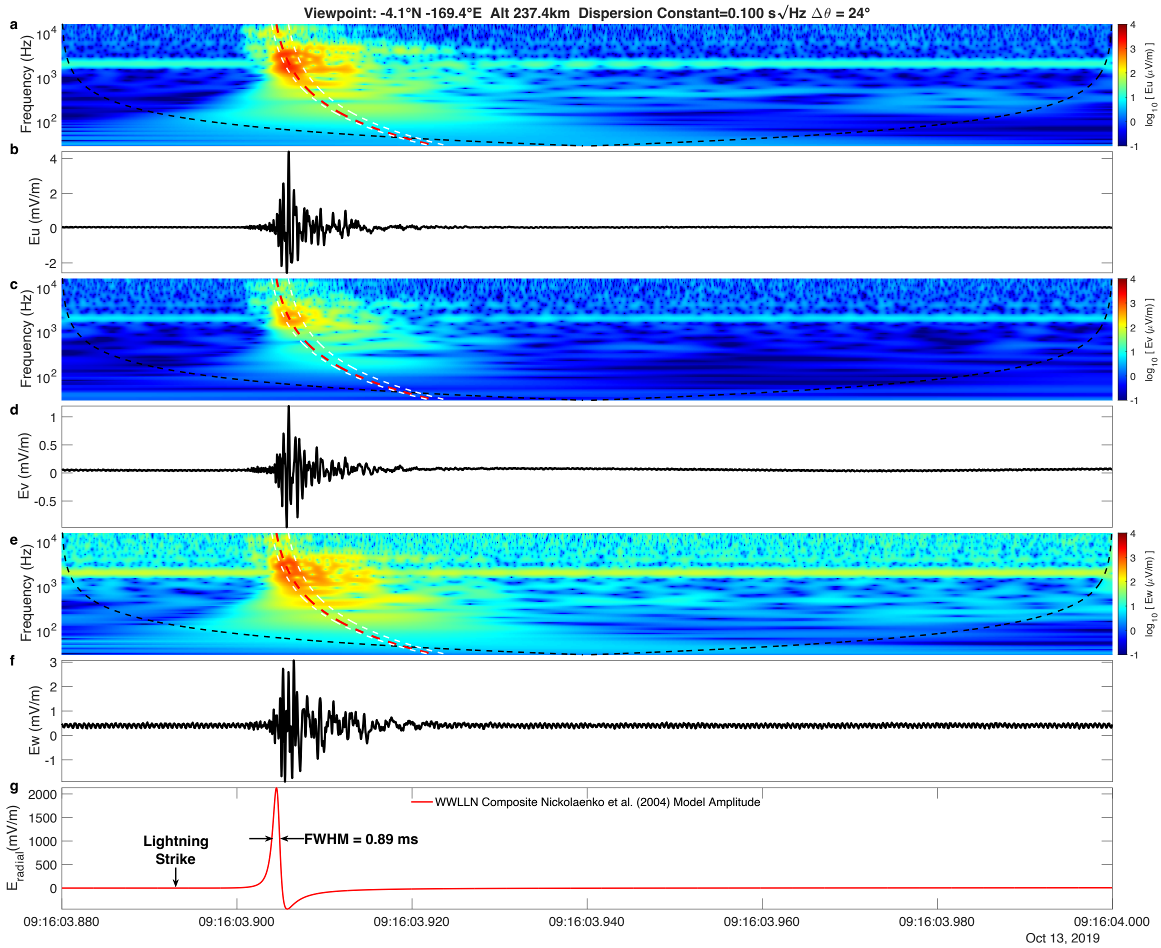

Figure S2. A closeup of the low dispersion event corresponding to the lightning strike at 9:16:03.389 shown in Figure **5** is displayed. The Nickolaenko et al. (2004) model radial electric field is plotted in **S2g**, with the strike time and width of the peak indicated. The dispersion curves for the *DC* value listed in the figure title are superimposed on the scalograms for the three components of the electric field in **S2a**, **S2c** and **S2e**. The electric fields as a function of time are plotted in **S2b**, **S2d** and **S2f**. As for Figure **11** in the main text, the red dashed line is the dispersion curve using the WWLLN measured time with a propagation speed through the EIWG of 245 Mm/s, while the white dashed lines are dispersion curves using the two GLM measured group times.

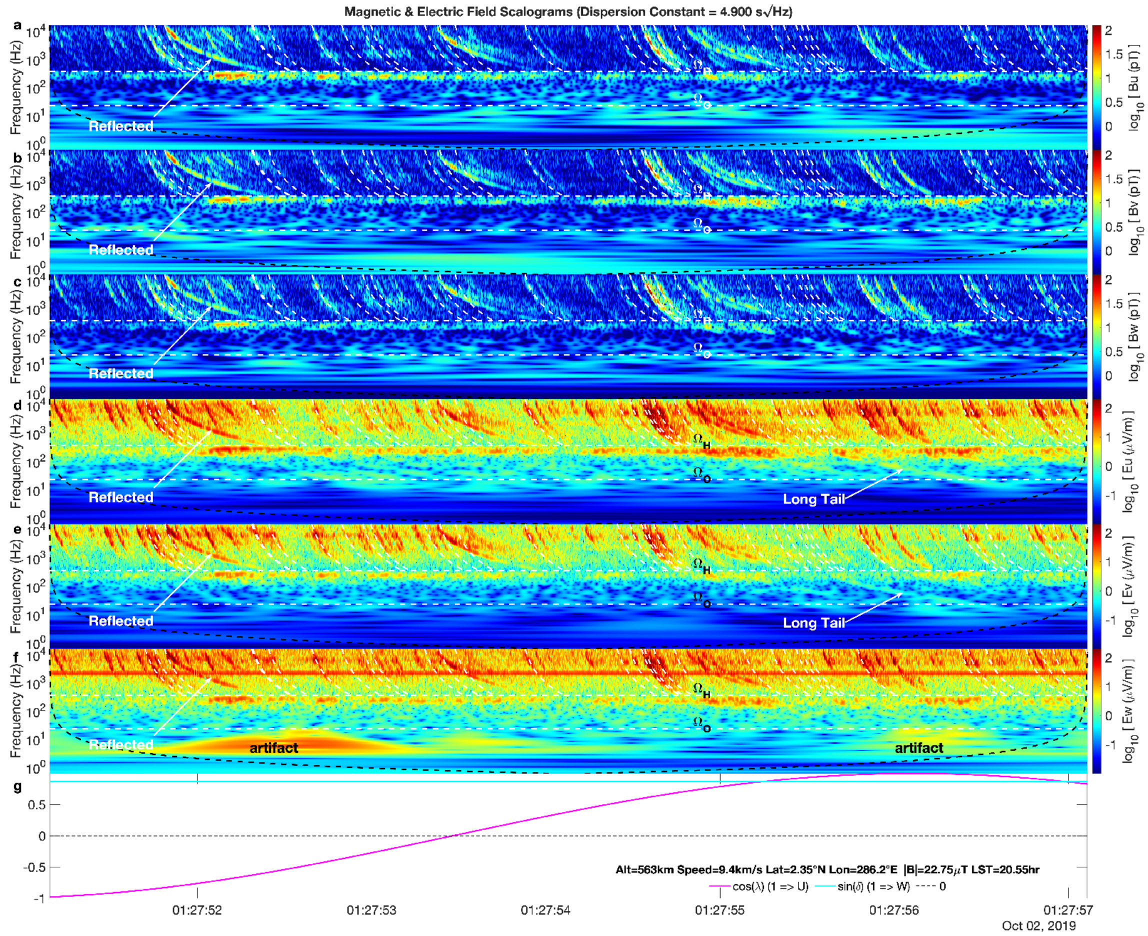

Figure S3. Scalograms from a single burst acquisition over a South American thunderstorm are plotted with the same layout as Figure **5**. In this case many whistlers having nearly identical dispersion constants (the dashed lines shown assume the *DC* value listed in the figure title) are seen. In addition, only a few echo whistlers, such as the example marked "Reflected", with significantly larger dispersion are seen.

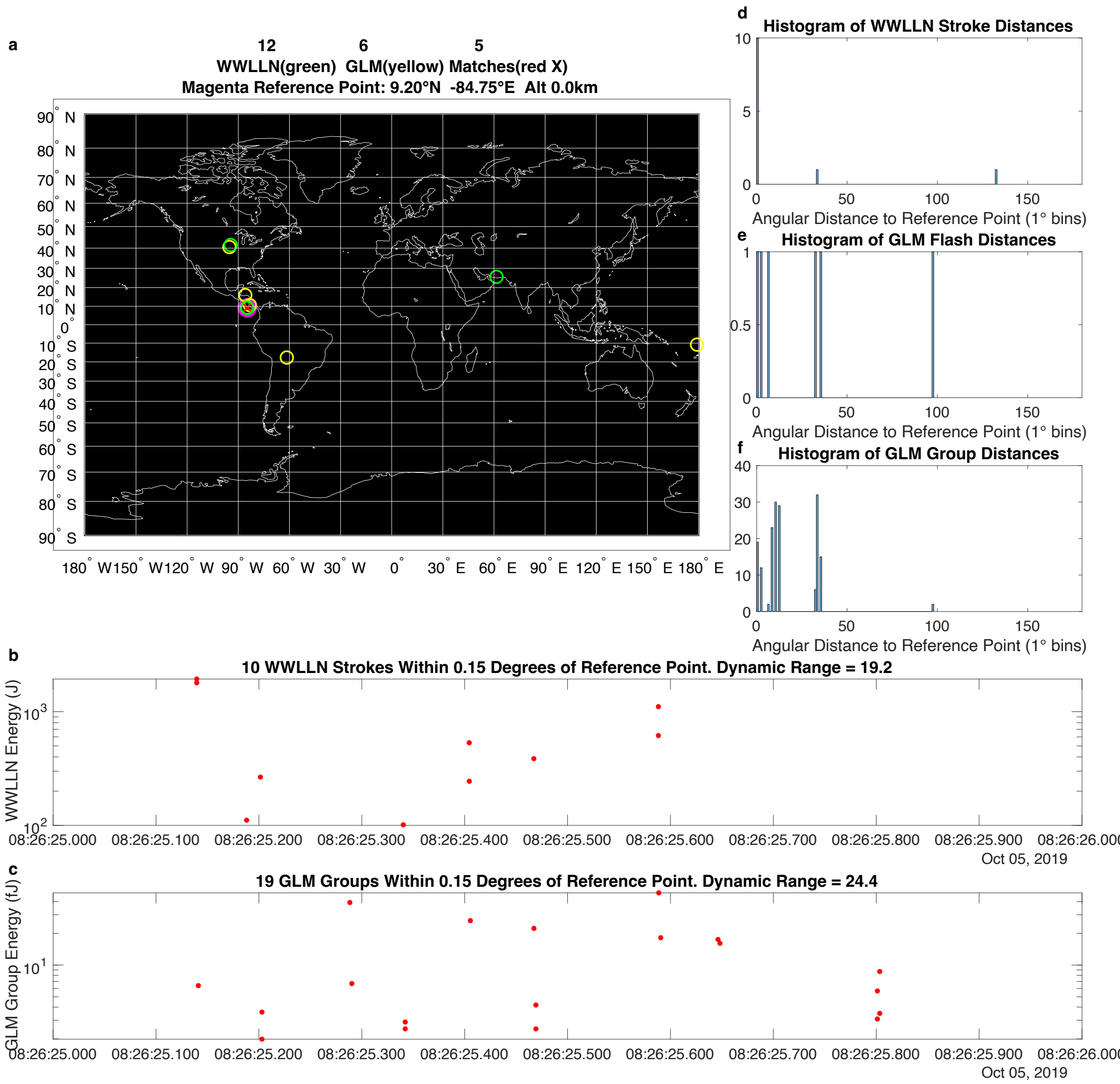

Figure S4. The single lightning flash at 9.20°N 84.75°W and its associated GLM groups and WWLLN strokes are displayed. Every GLM detected group associated with this flash is plotted in **S4c** as the measured group intensity versus time. Every WWLLN stroke associated with this flash is plotted in **S4b** as the measured energy versus time. The locations of every WWLLN stroke and GLM group over the one second interval 8:26:25 to 8:26:26 are plotted in **S4a**. Histograms of the angular distances to the reference location for every WWLLN stroke during this second are plotted in **S4d**. Histograms of the distances for every GLM flash during this second are in **S4e**, while histograms of distances for every GLM group during this second are in **S4f**.

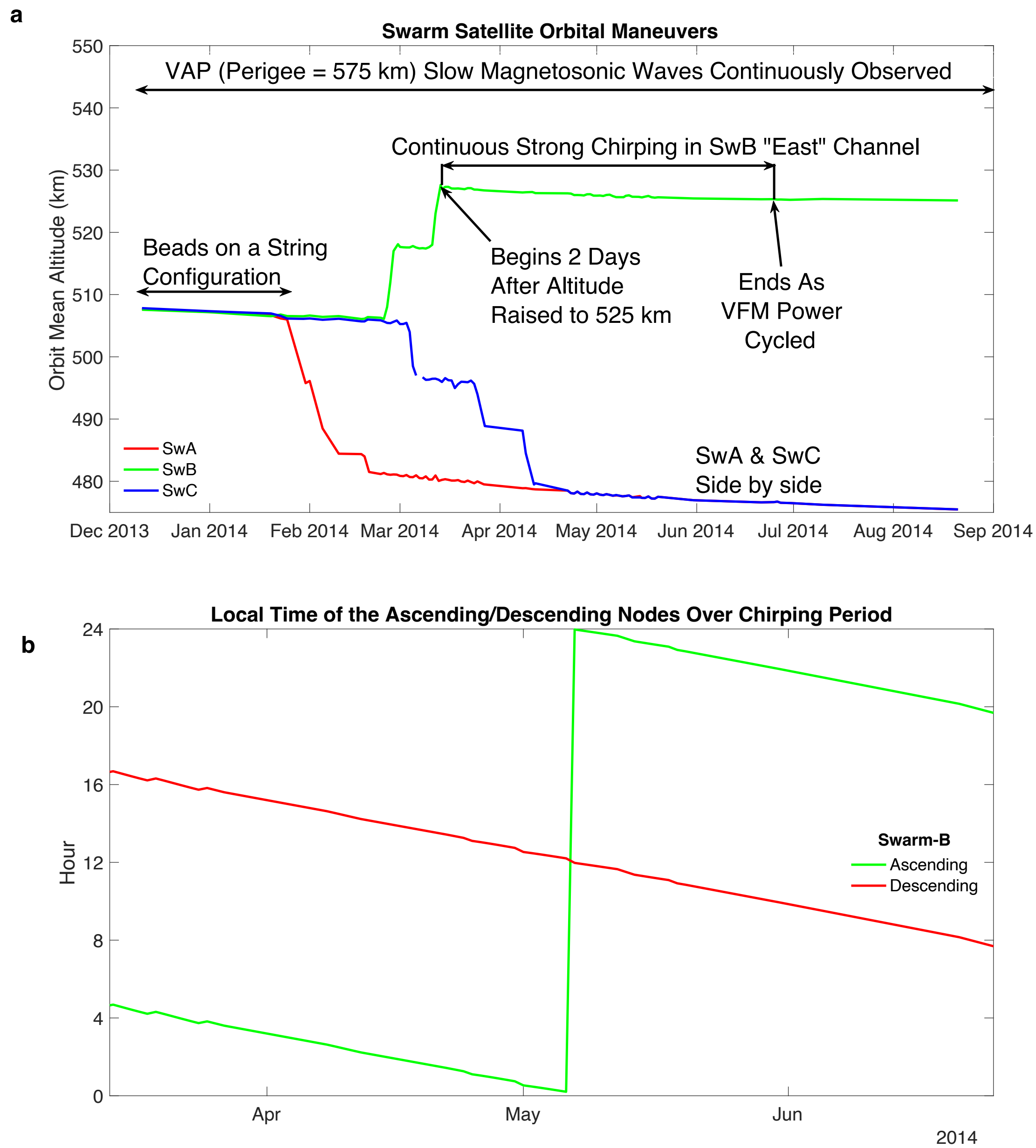

Figure S5. The initial development of the Swarm constellation configuration is illustrated. In **a**, the altitudes for SwA, B and C are shown as a function of time. In **b**, the local time of the ascending and descending nodes for the SwB satellite are shown.

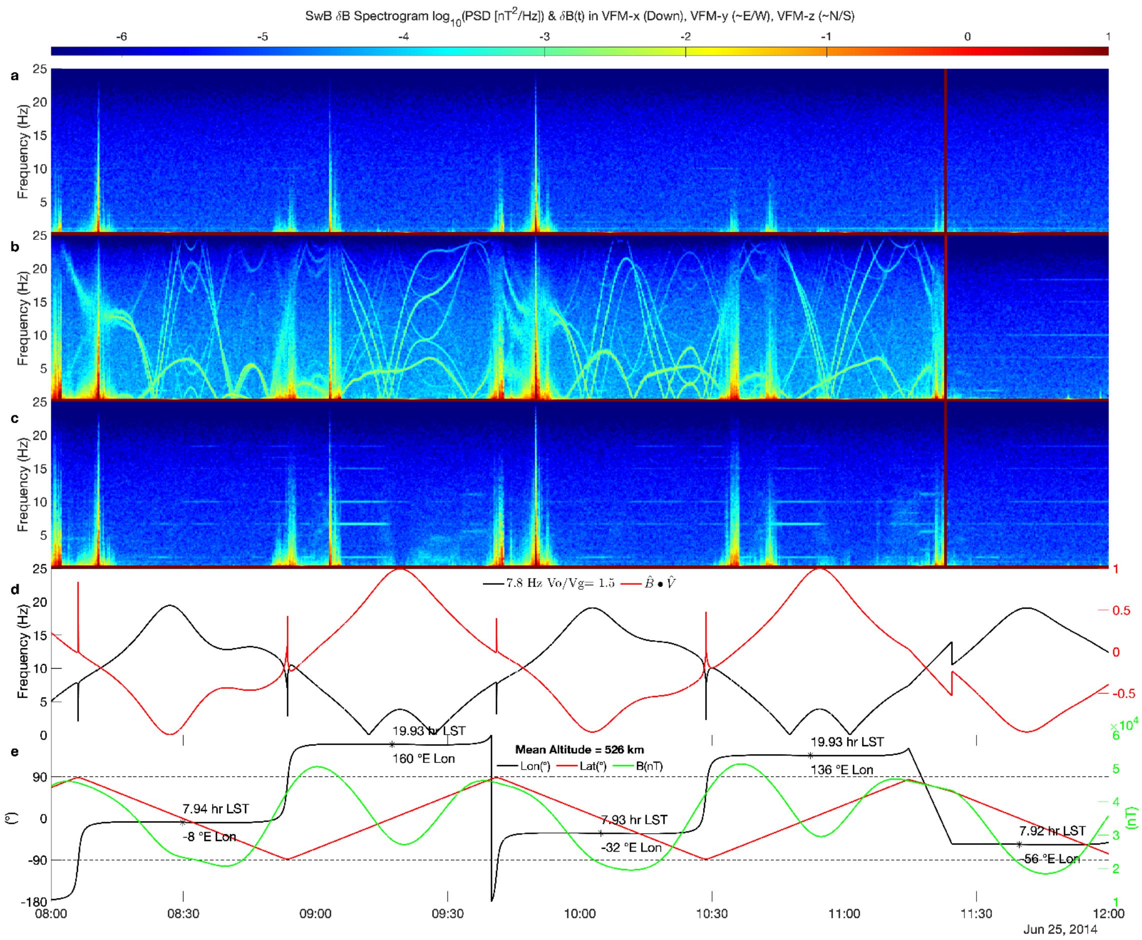

Figure S6. Spectrograms of data near the time of the cessation of chirping with the same layout as Figure **14** (except without the magnitude of VFM_y) are shown.

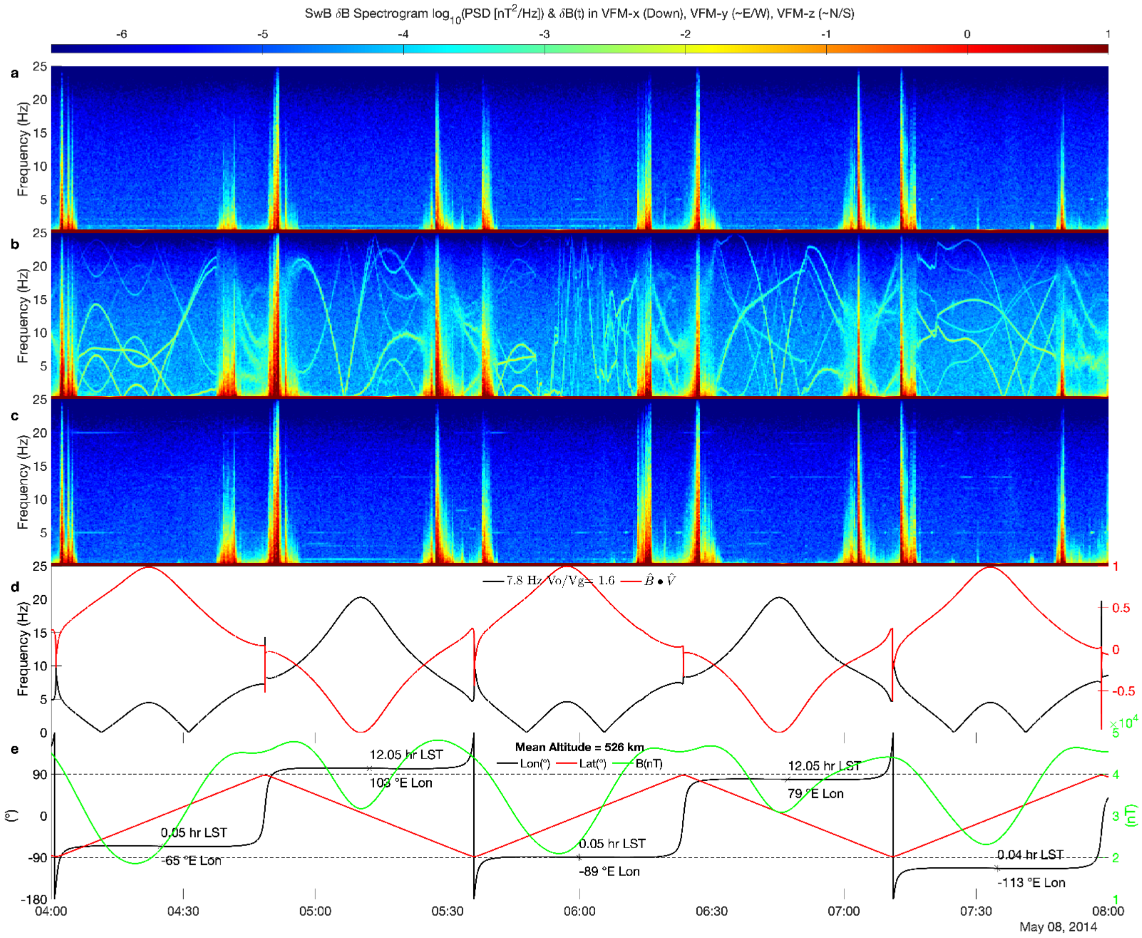

Figure S7. VFM spectrograms are shown near the first yaw slew maneuver. The layout is the same as the previous figure.

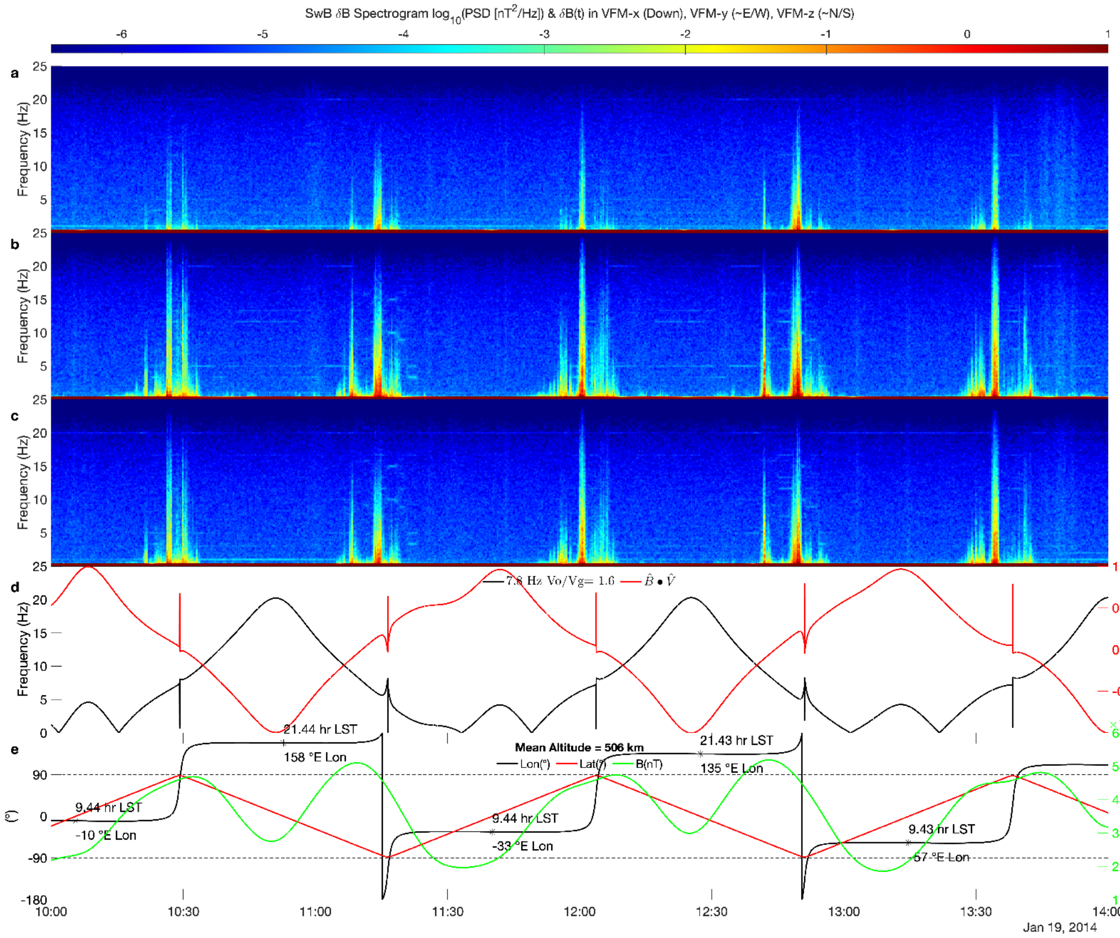

Figure S8. VFM spectrograms from around the time of a strong ASM whistler at 11:30:57. The layout is the same as the previous figure.